

**This item is the archived peer-reviewed author-version of:**

Understanding the activation of anionic redox chemistry in  $\text{Ti}^{4+}$ -substituted  $\text{Li}_2\text{MnO}_3$  as a cathode material for Li-ion batteries

**Reference:**

Paulus Andreas, Hendrickx Mylène, Mayda Bacaksiz Selma, Batuk Maria, Reekmans Gunter, von Holst Miriam, Elen Ken, Abakumov Artem M., Adriaensens Peter, Lamoen Dirk, ....- Understanding the activation of anionic redox chemistry in  $\text{Ti}^{4+}$ -substituted  $\text{Li}_2\text{MnO}_3$  as a cathode material for Li-ion batteries  
ACS applied energy materials - ISSN 2574-0962 - 6:13(2023), p. 6956-6971  
Full text (Publisher's DOI): <https://doi.org/10.1021/ACSAEM.3C00451>  
To cite this reference: <https://hdl.handle.net/10067/1981600151162165141>

# Understanding the activation of anionic redox chemistry in $\text{Ti}^{4+}$ -substituted $\text{Li}_2\text{MnO}_3$ as a cathode material for Li-ion batteries

Andreas Paulus<sup>a,b\*</sup>, Mylène Hendrickx<sup>c</sup>, Selma Mayda<sup>c</sup>, Maria Batuk<sup>c</sup>, Gunter Reekmans<sup>d</sup>, Miriam von Holst<sup>a</sup>, Ken Elen<sup>a,b</sup>, Artem M. Abakumov<sup>e,c</sup>, Peter Adriaensens<sup>d</sup>, Dirk Lamoen<sup>c</sup>, Bart Partoens<sup>f</sup>, Joke Hadermann<sup>c</sup>, Marlies K. Van Bael<sup>a,b</sup> and An Hardy<sup>a,b\*</sup>

<sup>a</sup>Hasselt University, Institute for Materials Research (imo-imomec) and imec, division imomec, Materials Chemistry, DESINE group, Agoralaan Gebouw D, 3590 Diepenbeek, Belgium

<sup>b</sup>EnergyVille, Thor Park 8320, 3600 Genk, Belgium

<sup>c</sup>University of Antwerp, Electron Microscopy for Materials Science (EMAT), Groenenborgerlaan 171, 2020 Antwerpen, Belgium

<sup>d</sup>Hasselt University, Institute for Materials Research (imo-imomec), NMR group, Agoralaan Gebouw D, 3590 Diepenbeek, Belgium

<sup>e</sup>Center for Energy Science and Technology, Skolkovo Institute of Science and Technology, 3 Nobel Street, Moscow 143026, Russia

<sup>f</sup>University of Antwerp, Condensed Matter Theory (CMT), Groenenborgerlaan 171, 2020 Antwerpen, Belgium

\*Email: andreas.paulus@uhasselt.be

Email: an.hardy@uhasselt.be

## Abstract

Layered Li-rich oxides, demonstrating both cationic and anionic redox chemistry being used as positive electrodes for Li-ion batteries, have raised interest due to their high specific discharge capacities exceeding 250 mAh/g. However, irreversible structural transformations triggered by anionic redox chemistry result in pronounced voltage fade (i.e. lowering the specific energy by a gradual decay of discharge potential) upon extended galvanostatic cycling. Activating or suppressing oxygen anionic redox through structural stabilization induced by redox-inactive cation substitution is a well-known strategy. However, less emphasis has been put on the correlation between substitution degree and the activation/suppression of the anionic redox. In this work,  $\text{Ti}^{4+}$ -substituted  $\text{Li}_2\text{MnO}_3$  was synthesized via a facile solution-gel method.  $\text{Ti}^{4+}$  is selected as a dopant as it contains no partially filled d-orbitals. Our study revealed that the layered “honeycomb-ordered”  $C2/m$  structure is preserved when increasing the Ti content to  $x=0.2$  in the  $\text{Li}_2\text{Mn}_{1-x}\text{Ti}_x\text{O}_3$  solid solution, as shown by electron diffraction and aberration-corrected scanning transmission electron microscopy. Galvanostatic cycling hints at a delayed oxygen release, due to an improved reversibility of the anionic redox, during the first 10 charge-discharge cycles for the  $x=0.2$  composition as compared to the parent material ( $x=0$ ), followed by pronounced oxygen redox activity afterwards. The latter originates from a low activation energy barrier towards O-O dimer formation and Mn migration in  $\text{Li}_2\text{Mn}_{0.8}\text{Ti}_{0.2}\text{O}_3$ , as deduced from first-principles molecular dynamics (MD) simulations for the “charged” state. Upon lowering the Ti substitution to  $x=0.05$ , the structural stability was drastically improved based on our MD analysis, stressing the importance of carefully optimizing the substitution degree to achieve the best electrochemical performance.

**Keywords:** Lithium-ion batteries,  $\text{Li}_2\text{MnO}_3$  positive electrode material, Transition metal substitution, Anionic redox chemistry, Delayed oxygen release

## Introduction

Layered Li-rich oxide positive electrode (cathode) materials for Li-ion batteries, showing both cationic and anionic redox chemistry, have drawn interest due to their high specific discharge capacities exceeding 250 mAh/g when the upper potential is above 4.5 V vs.  $\text{Li}^+/\text{Li}$ . This

capacity is significantly higher than the practical discharge capacity of about 145 mAh/g of the current commercially widely employed  $\text{LiCoO}_2$ .<sup>1</sup> Those layered Li-rich oxides are composed of alternating lithium and transition metal layers, in which part of the transition metal cations have been replaced by lithium. A characteristic of Li-rich oxides is the presence of localized oxygen non-bonding states. Those localized pseudo non-bonding O 2p states can be attributed to the absence of  $\sigma$ -type overlap with the transition metal 3d orbitals and mostly ionic Li-O bonding due to only a small overlap of O 2p and Li 2s orbitals. Upon oxidation of oxygen, electrons are most likely to be removed from this O 2p(NB) non-bonding states after the  $(\text{M}-\text{O})^*$  (M = transition metal) antibonding band is emptied, as the O 2p(NB) band is located above the M-O bonding band. This results in higher structural stabilization as compared to oxides where the additional electrons, after emptying the  $(\text{M}-\text{O})^*$  antibonding bands, can exclusively come from the M-O bonding bands.<sup>2,3</sup> The contribution of these O 2p(NB) states explains the higher reversible capacities for Li-rich oxides.<sup>4</sup>

A well-investigated class of layered Li-rich oxides showing anionic redox chemistry comprises the lithium-rich/manganese-rich lithium nickel manganese cobalt oxides (LMR-NMC,  $x\text{Li}_2\text{MnO}_3-(1-x)\text{LiMO}_2$  (M = Mn, Ni, Co)).<sup>5,6,7</sup> In the crystal structure of the end-member  $\text{Li}_2\text{MnO}_3$ , lithium replaces 33% of manganese in the transition metal layer resulting in a mixed Li-Mn layer with honeycomb-like ordering, hereafter denoted as the  $\text{LM}_2$  layer.<sup>8,9,10</sup> Therefore,  $\text{Li}_2\text{MnO}_3$  is often represented as  $\text{Li}(\text{Li}_{1/3}\text{Mn}_{2/3})\text{O}_2$ . Manganese is exclusively present in a 4+ oxidation state in pristine  $\text{Li}_2\text{MnO}_3$ . As the  $\text{Mn}^{5+}/\text{Mn}^{4+}$  redox couple is positioned below the top of the M-O bonding band having essentially O 2p character, oxygen should be oxidized first, turning  $\text{Mn}^{4+}$  to be electrochemically inactive in  $\text{Li}_2\text{MnO}_3$ . Despite this,  $\text{Li}_2\text{MnO}_3$  demonstrates prominent electrochemical activity upon galvanostatic cycling when charged to potentials above about 4.5 V vs.  $\text{Li}^+/\text{Li}$ . This unusual redox activity of  $\text{Li}_2\text{MnO}_3$  has been attributed to the contribution of anionic redox chemistry of the oxygen sublattice. This causes an irreversible structural transformation from the initial layered structure to a spinel-like motif and eventually a disordered rock salt-type structure. As a result, a deterioration of the electrochemical performance (i.e. resulting in voltage fade and capacity fade) takes place.<sup>10,11,12</sup> Structural transformations, caused by irreversible anionic redox chemistry, result in pronounced voltage fade (i.e. lowering the specific energy by a gradual decay of discharge potential) upon extended galvanostatic cycling that is commonly observed for 3d metal-based Li-rich oxides.

Several authors probed the origin of the anionic redox chemistry in  $\text{Li}_2\text{MnO}_3$ .<sup>13,9,10,14,15,16</sup> Despite the exact mechanisms behind anionic redox chemistry in layered Li-rich oxide materials for Li-ion batteries is still debatable, theoretical calculations indicate that the amount of holes created in the O 2p(NB) band during electron removal is strongly correlated with the relative energy level of the O 2p non-bonding states. The relative energy of the localized non-bonding oxygen states is mainly influenced by the electrostatic field induced by their local ionic environment.<sup>17</sup> The electrostatic field is impacted by the charge distribution in the crystal, or in other words by the M-O bond covalency, which is different for 3d, 4d and 5d transition metals.<sup>1,2,17</sup> The lower Madelung potential caused by lower charges of cations in the direct vicinity of an oxygen anion will result in a higher energy of the ligand (oxygen) bands.<sup>17</sup> As the octet rule is not fulfilled anymore, oxygen anions after the removal of electrons from their O 2p non-bonding states are very unstable. By recombining those unstable oxygen anions, (O-

O)<sup>n-</sup> (peroxide-like (O<sub>2</sub><sup>2-</sup>) and superoxide-like (O<sub>2</sub><sup>-</sup>)) dimer species are formed.<sup>17</sup> Those species are characterized by a short O-O distance. In this process, the electron desaturated O 2p bands of those unstable oxygen anions are separated in distinct  $\sigma$ ,  $\pi$ ,  $\pi^*$  and  $\sigma^*$  bands. The calculated O-O bond shortening together with the Mn-O bond elongation at sufficiently high charging potentials hints at partial de-coordination of O-O dimers. The stabilization of the created O<sub>2</sub><sup>n-</sup> species is weak due to a lack of Mn-O covalency, leading to oxygen release<sup>18</sup> and reduction of Mn<sup>4+</sup> to Mn<sup>3+</sup> during the subsequent discharge. The O<sub>h</sub> → T<sub>h</sub> migration of Mn<sup>3+</sup> at V>4.1 V vs. Li<sup>+</sup>/Li, experimentally observed by neutron powder diffraction, can be associated with the Jahn-Teller instability of octahedrally coordinated Mn<sup>3+</sup> cations possessing a d<sup>4</sup> high spin electron configuration.<sup>1</sup> In subsequent charge-discharge cycles, Mn<sup>3+</sup> is able to contribute to the capacity because of the activated Mn<sup>3+</sup>/Mn<sup>4+</sup> redox couple.

Having a closer look at the O-O dimer formation, by means of a theoretical framework, Seo *et al.*<sup>19</sup> showed that rotation to hybridize oxidized Li-O-Li states of two adjacent oxidized oxygens, required to form (O<sub>2</sub>)<sup>n-</sup>-like species, is facilitated when the M-O bonds of those oxygens are less directional (i.e. M does not contain partially filled d orbitals). To our knowledge, it is not revealed yet if partial replacement of Mn<sup>4+</sup> by an isovalent 3d transition metal cation containing no partially filled d orbitals would effectively favour O-O dimer formation and if this would result in a lower/higher extent of oxygen loss or not. In order to provide a detailed answer to the question, in this work we assessed anionic redox chemistry for Ti<sup>4+</sup>-substituted Li<sub>2</sub>MnO<sub>3</sub> by a combined experimental and theoretical approach. Ti<sup>4+</sup> has been selected to substitute Mn<sup>4+</sup> due to the absence of partially filled 3d orbitals and an ionic radius close to Mn<sup>4+</sup> (i.e. facile to form a solid solution).<sup>20</sup>

## Experimental

### Synthesis procedure

Li<sub>2</sub>Mn<sub>1-x</sub>Ti<sub>x</sub>O<sub>3</sub> was prepared via an aqueous solution-gel method. Dissolving respectively Li citrate hydrate (Li<sub>3</sub>C<sub>6</sub>H<sub>5</sub>O<sub>7</sub>·xH<sub>2</sub>O, Sigma Aldrich, 97%) and Mn(II) nitrate hydrate (Mn(NO<sub>3</sub>)<sub>2</sub>·xH<sub>2</sub>O, Sigma Aldrich, 98%) in Milli-Q water resulted in Li citrate and Mn(NO<sub>3</sub>)<sub>2</sub> precursors. An aqueous Ti<sup>4+</sup> precursor solution was prepared by adjusting the protocol described by Hardy *et al.*<sup>21</sup> An amount of 6 mL of Ti(IV) isopropoxide (Ti[OCH(CH<sub>3</sub>)<sub>2</sub>]<sub>4</sub>, Acros Organics, 98+%) has been added to 60 mL of Milli-Q H<sub>2</sub>O. The obtained titanium oxyhydroxide precipitate was washed with water by means of vacuum filtration. In the meantime, 3.84 g of citric acid (C<sub>6</sub>H<sub>8</sub>O<sub>7</sub>, Sigma Aldrich, 99%) was dissolved in 10 mL of Milli-Q H<sub>2</sub>O and subsequently mixed with 2 mL hydrogen peroxide (H<sub>2</sub>O<sub>2</sub>, Merck, 35%). This mixture was added to the washed precipitate and stirred at 60 °C to dissolve the precipitate. Hereafter, the pH was increased till 6.5 by dropwise addition of ammonia (NH<sub>3</sub>, Merck, extra pure, 32%). Next, the precursor was heated at 108 °C for about 10 min. After cooling down to room temperature the pH was increased by the dropwise addition of NH<sub>3</sub> till 7. After vacuum filtration and adjusting the total volume to 100 mL, the final 0.2 M Ti<sup>4+</sup> solution precursor was obtained. Citric acid (CA, Sigma Aldrich, 99%) was added to an aqueous mixture containing stoichiometric amounts of Li citrate, Mn(NO<sub>3</sub>)<sub>2</sub> and Ti<sup>4+</sup> solution precursors in a 2:1

CA:Mn(NO<sub>3</sub>)<sub>2</sub> molar ratio. As at high calcination temperatures a potential loss of volatile Li-containing species was anticipated, a lithium excess of 10 molar % was used. After dissolving the citric acid, the pH was set at ~7 by dropwise addition of NH<sub>3</sub> (NH<sub>3</sub>, Merck, extra pure, 32%). Thereafter, the mixture was refluxed at 80 °C for 1 hour. After the reflux step, the mixture was gelled under atmospheric conditions at 60 °C overnight in an oven. The gel was pre-calcined at 200 °C under atmospheric conditions. The grinded pre-calcined powder was calcined again by applying the following procedure: 500 °C for 5 hours under dynamic O<sub>2</sub> atmosphere (Air Liquide, industrial), cooling down and grinding for 15 min by mortar and pestle followed by 900 °C for 12 hours under dynamic dry air atmosphere (DA, Air Liquide, 99.999% purity) during the heating step (DA gas bottle was closed after reaching a furnace temperature of 900 °C). Both thermal treatment steps were performed in a tube furnace. A heating rate of 5°C/min was applied for heating up to respectively 500 °C and 900 °C. Li<sub>2</sub>MnO<sub>3</sub> was prepared via the same procedure as described above while excluding the addition of Ti<sup>4+</sup> solution precursor. The obtained end products were grinded and stored sealed in glass vials in an Argon-filled glovebox for further use.

### **Chemical and physical characterization of pristine materials**

The concentrations of the monometal precursors and Li:Mn elemental ratio in the end products were determined by atomic emission spectroscopy with inductively coupled plasma (ICP-AES, Optima 3300 DV, PerkinElmer). Powder X-ray diffraction (PXRD) patterns were acquired on a Huber G670 Guinier diffractometer operated with Co K<sub>α1</sub> radiation. Le Bail refinement on the PXRD data was conducted making use of the Jana2006 software package.<sup>22</sup> Raman spectroscopy measurements were performed with a Horiba Jobin Yvon T64000 triple spectrometer equipped with a BXFM Olympus microscope (100x magnification), a Horiba Jobin Yvon Symphony CCD detector and a 488 nm Lexel SHG laser operated below 20 mW. The energy-dispersive X-ray mapping in a scanning transmission electron microscopy mode (STEM-EDX) was performed on a Thermo Fisher Osiris transmission electron microscope equipped with a Super-X detector and operated at 200 kV. The selected area electron diffraction (SAED) patterns were collected on a Thermo Fisher Tecnai G2 transmission electron microscope operated at 200 kV. The high angle annular dark field scanning transmission electron microscopy (HAADF-STEM) images were acquired with a probe aberration-corrected Thermo Fisher Titan 80-300 “cubed” microscope operated at 300 kV. The HAADF-STEM line profiles were fitted using the program Fityk<sup>23</sup>. The preparation of the pristine samples for SAED and HAADF-STEM included crushing the powders in ethanol and subsequently dispersing them in this liquid using an ultrasonic bath. For the particle size distribution analysis and STEM-EDX mapping, the powder was only dispersed in ethanol using ultrasonic bath without crushing. A few droplets of the obtained suspension were deposited on a Cu TEM grid covered with a holey carbon layer. <sup>7</sup>Li solid-state MAS (Magic Angle Spinning) NMR spectra were acquired on an Agilent VNMR DirectDrive 400MHz spectrometer (9.4 T wide bore magnet) equipped with a T3HX 3.2 mm probe. MAS was performed at 20 kHz and the signal of LiCl was used to calibrate the lithium chemical shift scale (0 ppm). To distinguish between an isotropic chemical shift and the spinning sidebands flanking either side at distances that are multiples of the spin rate, spectra of the same samples were also recorded at spin rate of 17 kHz

and 23 kHz. Only signals whose position is independent of the spin rate are isotropic peaks; all other peaks are spinning sidebands. Acquisition parameters used were the following: a spectral width of 625 kHz, a 90° pulse length of 2.5  $\mu$ s, an acquisition time of 4 ms, a recycle delay time of 2 s, and 800 accumulations.

## **Electrochemical characterization**

The final products were characterized electrochemically in a coin cell configuration. To prepare a coating, the active cathode material was mixed with carbon black (Imerys, Super C65) and polyvinylidene difluoride (PVDF, Alfa Aesar) as a binder in *N*-methyl pyrrolidone (NMP, Alfa Aesar) solvent in a weight ratio of 80:10:10. This mixture was ball milled at 500 rpm to obtain a slurry, which was deposited by tapecasting on an aluminum current collector aiming at a wet coating thickness of  $\sim$ 150  $\mu$ m. Cathode punches were dried in a vacuum oven (Büchi) overnight and inserted under vacuum in an Argon-filled glovebox. As an anode, Li metal (Sigma Aldrich, 99.9% trace metals purity) was used and as a separator a trilayered membrane (Celgard 2400) was applied to obtain coin cell-type half cells. 1M LiPF<sub>6</sub> in EC:DMC (Sigma Aldrich, 50/50 (v/v)% ethylene carbonate:dimethyl carbonate) was used as the electrolyte. Galvanostatic cycling was performed between 2.0 and 4.8 V vs. Li<sup>+</sup>/Li at C-rates of C/20 (two initial cycles) and C/10 (50 subsequent cycles) using a Bio-Logic BCS-805 battery tester. The C-rate was calculated based on an assumed theoretical capacity of 250 mAh/g. In order to enhance the wetting of the electrode and separator compounds by the electrolyte, a resting period of 24 hours was respected between coin cell assembly and electrochemical testing.

## **Physical characterization after galvanostatic cycling**

Coin cells were disassembled in an Argon-filled glovebox. Cathode punches were washed three consecutive times with dimethyl carbonate to remove the remaining electrolyte. During the TEM sample preparation, the powder was scratched from the cathode punch and crushed. Then, a Cu TEM grid covered with a holey carbon layer was dipped into the dry powder. Via a vacuum transfer holder, the sample on the Cu TEM grid has been transferred to the TEM, excluding contact with ambient atmosphere.

## **First-principles calculations**

Calculations were performed within the framework of density functional theory (DFT)<sup>24,25</sup> using the PBE functional<sup>26</sup> including spin polarization with the VASP<sup>27,28,29,30</sup> code. The on-site Coulomb interaction (PBE+U) was used to describe the strongly correlated electrons of the Mn and Ti atoms. The Hubbard effective *U* values for Mn and Ti were taken as 3.9 eV<sup>31</sup> and 4.2 eV<sup>32,33,34</sup> respectively. The energy cutoff was set to 500 eV for the plane-wave basis set. The interaction between valence and core electrons was treated using the projector augmented wave (PAW)<sup>35</sup> method. The atomic positions were relaxed until the residual forces on the atoms were less than 0.01 eV/Å and the total energy was converged to within 10<sup>-2</sup> meV. In these calculations, a 2x2x2 supercell of the primitive cell with 96 atoms was used.

In order to examine the O-O dimer formation and the displacement of the Mn atoms in the Ti-substituted structures, also first-principles molecular dynamics (MD) simulations were performed within a 2x2x2 supercell of delithiated structures with 576 atoms. A time step of 1 fs was used and the calculations were performed at T=300 K and 1000 K. The temperature was tuned by the Nosé-Hoover<sup>36,37</sup> thermostat.

## Results and discussion

### Structural characterization of pristine materials

Ti<sup>4+</sup> substitution has already been successfully executed for Li<sub>2</sub>MnO<sub>3</sub> (followed by carbothermal reduction to reduce manganese)<sup>38,39</sup> and LMR-NMC (with composition Li<sub>1.2-x</sub>Ti<sub>x</sub>Co<sub>0.13</sub>Mn<sub>0.54</sub>Ni<sub>0.13</sub>O<sub>2</sub>)<sup>18</sup>. However, to our knowledge no study is available yet on the detailed correlation between Ti<sup>4+</sup> for Mn<sup>4+</sup> substitution degree and crystal structure. This section is dedicated to the structure and homogeneity of Li<sub>2</sub>Mn<sub>1-x</sub>Ti<sub>x</sub>O<sub>3</sub>. Powder X-ray diffraction (PXRD) patterns of pristine Li<sub>2</sub>MnO<sub>3</sub> (LMO), Li<sub>2</sub>Mn<sub>0.9</sub>Ti<sub>0.1</sub>O<sub>3</sub> (LMTO-1), Li<sub>2</sub>Mn<sub>0.8</sub>Ti<sub>0.2</sub>O<sub>3</sub> (LMTO-2) and Li<sub>2</sub>Mn<sub>0.7</sub>Ti<sub>0.3</sub>O<sub>3</sub> (LMTO-3) are depicted in **Figure 1**. The sharp diffraction peaks indicate that the materials are well crystallized. No secondary phases were detected, and all peaks correspond to Li<sub>2</sub>MnO<sub>3</sub>-type phases.<sup>7</sup> The diffraction peaks between 20° and 25° 2 $\theta$  present for all the samples can be ascribed to the honeycomb-type Li-Mn ordering in a monoclinic layered Li<sub>2</sub>MnO<sub>3</sub> type structure.<sup>8,9,10,11</sup> The well-defined superlattice reflections in the LMO and LMTO-3 PXRD patterns indicate that upon replacing up to 30% of Mn<sup>4+</sup> by Ti<sup>4+</sup> the honeycomb ordering in the mixed LM<sub>2</sub> layer has been maintained. The peak shift, indicated by the dashed line in **Figure 1**, to lower 2 $\theta$  values upon increasing the degree of Ti<sup>4+</sup> substitution indicates an increase in unit cell parameters. The unit cell parameters and volume refined with the C2/m symmetry by the Le Bail method are presented in **Table 1**. The PXRD patterns after fitting with the Le Bail method are depicted in the Supporting Information **Figure S1**. The increase in the unit cell parameters and volume upon raising the Ti<sup>4+</sup> content from x=0 to x=0.1 to x=0.2 is attributed to the larger ionic radius of Ti<sup>4+</sup> (0.605 Å) as compared to Mn<sup>4+</sup> (0.53 Å)<sup>40</sup>.

**Table 1.** Refined unit cell parameters and volume of Li<sub>2</sub>Mn<sub>1-x</sub>Ti<sub>x</sub>O<sub>3</sub>, LMO (x=0), LMTO-1 (x=0.1), LMTO-2 (x=0.2), LMTO-3 and (x=0.3).

	LMO	LMTO-1	LMTO-2	LMTO-3
<i>a</i> (Å)	4.92872(7)	4.94172(8)	4.95326(7)	4.96272(9)
<i>b</i> (Å)	8.5315(1)	8.5448(2)	8.5706(1)	8.5809(2)
<i>c</i> (Å)	5.0250(1)	5.0282(1)	5.03814(8)	5.0424(1)
$\beta$ (°)	109.207(1)	109.147(3)	109.326(1)	109.113(1)
<i>V</i> (Å <sup>3</sup> )	199.536(7)	200.573(6)	201.828(6)	202.758(7)

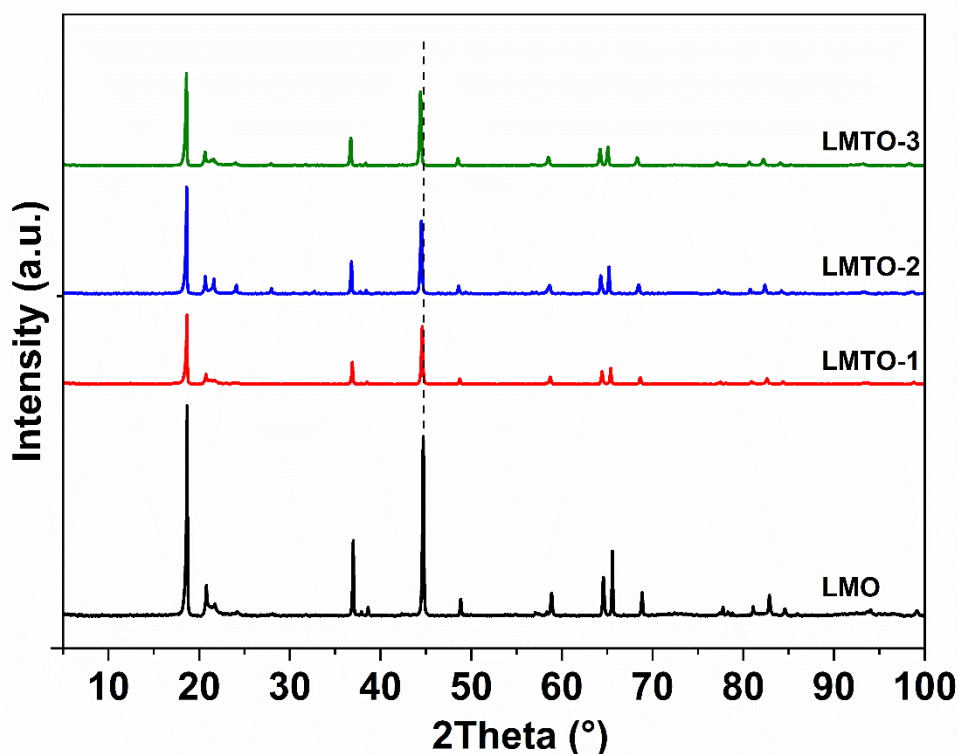


**Figure 1.** PXRD patterns of  $\text{Li}_2\text{Mn}_{1-x}\text{Ti}_x\text{O}_3$ : LMO ( $x=0$ ), LMTO-1 ( $x=0.1$ ), LMTO-2 ( $x=0.2$ ) and LMTO-3 ( $x=0.3$ ). The peak shift as a function of  $\text{Ti}^{4+}$  substitution degree  $x$  is indicated by the dashed line.

The HAADF-STEM images and corresponding STEM-EDX maps of the samples are shown in **Figure 2**. According to the images, the samples have similar morphologies. In all samples, the majority of the particles are smooth with an almost isotropic shape and there are also some particles that have an irregular shape and a rough surface. The size of the particles varies from around 200 nm to 1  $\mu\text{m}$ , with most of the smooth particles having a size of 400-600 nm. The corresponding size distributions are shown in **Figure S2** of the Supporting Information. A homogeneous distribution of Mn and O is observed for LMO. No particles without Mn were detected (i.e. particles consisting of  $\text{Li}_2\text{O}$  or  $\text{Li}_2\text{CO}_3$ ), which is in agreement with the ICP-AES analysis, confirming that the Li/Mn ratio equals the expected stoichiometry. The mixed (Mn/Ti) element map of LMTO-1 shows an overall homogeneous distribution of Ti and Mn, regardless the particle morphology; only a few Ti-enriched areas were observed. The expected and average relative percentages for Mn and Ti for the Ti-containing samples are summarized in **Table 2**. The LMTO-2 sample contains in general a uniform distribution of titanium and manganese within LMTO particles. For some particles, Ti segregation at the surface can be seen. Next to LMTO, a few particles showing only Ti and O peaks have been observed having a rod-like morphology (0.7-1.2  $\mu\text{m}$ ) and plate-like morphology (on average 2.5  $\mu\text{m}$ ). Some of those particles show a small amount of Mn, which can be related to doping or to overlap with an LMTO particle. The low Z number of Li does not allow a conclusion about the presence of Li from EDX. In the LMTO-3 sample, the distribution of Mn and Ti is less homogeneous than in other samples. Segregation of Ti was also observed at the surface of some particles. Also, for



LMTO-3 particles showing only Ti and O peaks were detected. An elemental map for LMTO-3, containing a particle for which only Ti and O peaks were detected, is included in the Supporting Information **Figure S3**.

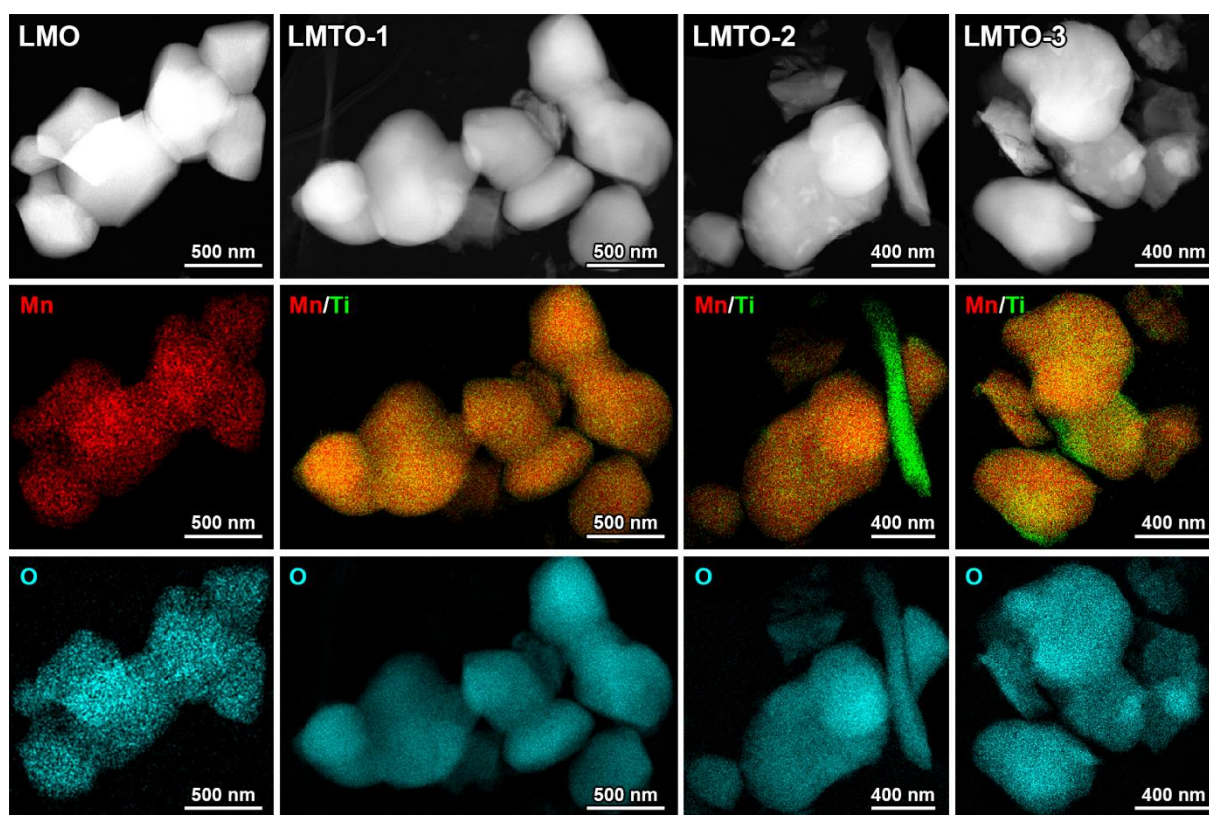


**Figure 2.** HAADF-STEM images and corresponding STEM-EDX mixed {Mn, Ti} and individual O elemental maps of representative particles of the LMO, LMTO-1, LMTO-2 and LMTO-3 samples.

**Table 2.** Expected and average experimentally determined relative concentrations of Mn and Ti in the LMTO samples.

	Expected Mn [at.%]	Expected Ti [at.%]	EDX Mn [at.%]	EDX Ti [at.%]
<b>LMTO-1</b>	90	10	91 (1)	9 (1)
<b>LMTO-2</b>	80	20	82 (1)	18 (1)
<b>LMTO-3</b>	70	30	74 (3)	26 (3)

The particles exclusively containing Ti and O observed via STEM-EDX for LMTO-2 and LMTO-3 could be composed of  $\text{TiO}_2$  or LTO ( $\text{Li}_x\text{Ti}_y\text{O}_z$ , e.g.  $\text{Li}_2\text{TiO}_3$ ). The three most common polymorphs of  $\text{TiO}_2$  are anatase, rutile and brookite. Raman spectroscopy is proven to be an excellent characterization technique to distinguish between these  $\text{TiO}_2$  polymorphs.<sup>41</sup> The Raman spectra of LMTO-1 and LMTO-2 together with the LMO reference spectrum are shown in **Figure S4**. LMTO-3 is excluded because of the lower homogeneity of the main LMTO phase. According to group theory, there exist 15 Raman-active vibration modes, 7  $A_g$  and 8  $B_g$  modes, for  $\text{Li}_2\text{MnO}_3$ . The  $A_g$  modes are caused by symmetric cation vibrations along the  $b$ -axis. The main  $A_g$  mode,  $A_{1g}$ , in the  $600\text{--}620\text{ cm}^{-1}$  Raman shift interval is attributed to symmetric M-

O vibrations.<sup>16</sup> All main peaks presented for all samples correspond to the  $\text{Li}_2\text{MnO}_3$ -type structure.

Because of the synthesis temperature of 900 °C,  $\text{TiO}_2$ , if present, is expected to have the stable rutile structure. The Raman spectrum of rutile is characterized by two strong main peaks at around 448  $\text{cm}^{-1}$  and 612  $\text{cm}^{-1}$  ascribed to respectively the  $E_g$  and  $A_{1g}$  normal modes of  $\text{TiO}_2$  and a moderately strong broad band with maximum at about 235  $\text{cm}^{-1}$ . This band cannot be unambiguously attributed to a normal mode of  $\text{TiO}_2$ , but can be most certainly ascribed to the disorder characteristic for the rutile's crystal structure.<sup>42</sup> The positions of the two main peaks overlap with those of the  $B_g$  and  $A_g$  normal modes of the  $\text{Li}_2\text{MnO}_3$  lattice. The absence of a broad band around 235  $\text{cm}^{-1}$  in the Raman spectra of the Ti-substituted  $\text{Li}_2\text{MnO}_3$  samples indicates that either  $\text{TiO}_2$  is not present as the rutile phase, or its content is below the detection limit of our Raman spectrometer. Peaks related to other polymorphs of  $\text{TiO}_2$  were also not detected. The Raman spectrum of the end-member  $\text{Li}_2\text{TiO}_3$  ( $x=1$  in  $\text{Li}_2\text{Mn}_{1-x}\text{Ti}_x\text{O}_3$ ) is characterized by four main normal modes at 358  $\text{cm}^{-1}$ , 409  $\text{cm}^{-1}$ , 430  $\text{cm}^{-1}$  and 668  $\text{cm}^{-1}$  respectively.<sup>43</sup> None of these modes were observed, indicating that  $\text{Li}_2\text{TiO}_3$  is not present or its quantity is below the detection limit. Also, no peaks related to other common LTO compositions were detected. Together with the average composition of the LMT-particles in agreement with the expected composition calculated from EDX, it is concluded that LTO or  $\text{TiO}_2$  observed in the HAADF-STEM elemental maps can be present in a low quantity only.

The LMO, LMTO-1 and LMTO-2 samples are comparatively assessed with SAED and HAADF-STEM. The LMTO-3 sample has been excluded from further characterization as the Mn and Ti elemental distribution determined by STEM-EDX is less homogeneous than for the other compositions. The SAED patterns for all samples confirm the monoclinic  $C2/m$  symmetry. Representative SAED patterns of the [100] and [010] zones of LMO, LMTO-1 and LMTO-2 are shown in **Figure 3**.

The HAADF-STEM images along these two main zones are displayed in **Figure 4** for the LMO and LMTO-2 samples. The [010] HAADF-STEM image of LMTO-1 is added to the Supporting Information **Figure S5**. As the intensity in the HAADF-STEM images is proportional to  $\sim Z^2$ , only the M atom columns are clearly visible, the oxygen columns are only vaguely observable and the Li columns produce too weak signal to be observed. For all samples, the [100]/[110] HAADF-STEM images demonstrate the honeycomb ordering in the  $\text{LM}_2$  layer, which is apparent by a pair of bright dots (atom columns containing Ti and Mn) separated by dark spaces (atom column containing Li). The [010] HAADF-STEM images show that the layered structure with alternating M and Li layers is preserved after Ti substitution, which is also confirmed by line profiles taken perpendicular to the layers.

The line profiles for the LMO, LMTO-1 and LMTO-2 samples are depicted in **Figure S7**, and the area of which the line profiles were taken are marked in **Figure S6**. The observed peaks in the line profiles are associated with both the M and O atom columns, which is confirmed by HAADF-STEM intensity simulations that are included in the Supporting Information, **Figure S11**. No significant differences are observed between the line profiles taken from the different pristine samples. Only a small additional peak at the lithium layer is observed in the line profile of the LMTO-1 sample, which means that some transition metals occupy positions in the lithium layer.

For all three samples, the representative SAED patterns and HAADF-STEM images are consistent with an O3 type of stacking, as in the  $\text{Li}_2\text{MnO}_3$  structure. No significant difference in the amount of stacking faults along the  $c$  direction is seen in the HAADF-STEM images. The stacking faults associated with the lateral displacements of the  $\text{LM}_2$  “honeycomb”-ordered layers are also apparent through the streaks along  $c^*$  of the [100] SAED patterns. However, as they can differ from particle to particle, it is difficult to compare their amount between samples. The occurrence of stacking faults of the  $\text{LM}_2$  layers is well-known for  $\text{Li}_2\text{MnO}_3$ , even when elevated synthesis temperatures have been applied.<sup>44</sup> In addition, some disorder in the honeycomb layers is observed, as indicated with arrows in the [100]/[110] HAADF-STEM image of the LMO sample.

Some of the observed particles for the LMO, LMTO-1 and LMTO-2 samples are twinned. An example is shown in the supporting information **Figure S8**, which shows domain formation within a single crystal of LMTO-1 with different orientations. The domains can be indexed considering the regular twin relations occurring for a symmetry decrease from the parent rock-salt structure  $Fm\bar{3}m$ , where M and Li are randomly distributed, to the honeycomb ordered layered  $C2/m$ , and are similar to those reported for lithium-rich manganese-rich NMC by Jarvis *et al.*<sup>45</sup> and Shukla *et al.*<sup>46</sup> The twin domains result in sharp reflections in the SAED patterns indicating that the domains are at least a few tens of nanometres in size. Those twin domains could have a potential influence on the electrochemical performance, but is beyond the scope of this manuscript.

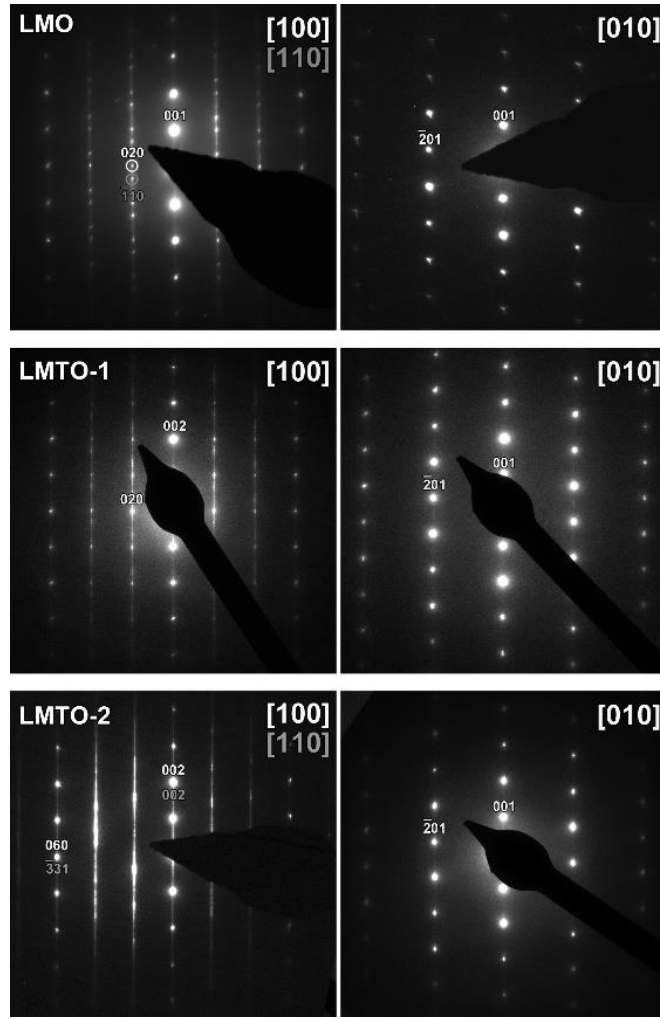


**Figure 3.** SAED patterns along the  $[100]/[110]$  and  $[010]$  zones of LMO, LMTO-1 and LMTO-2.

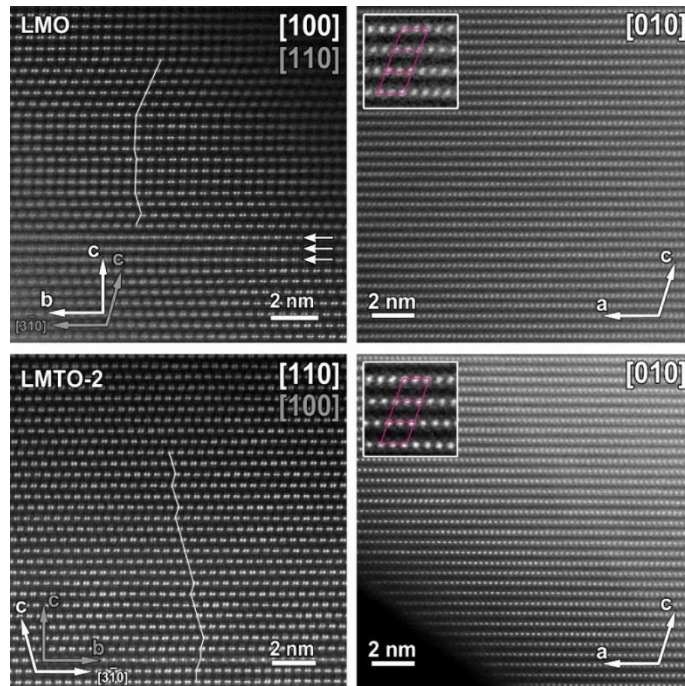


**Figure 4.** HAADF-STEM images along the  $[100]/[110]$  and  $[010]$  orientation of the LMO and LMTO-

2 samples. The white lines indicate the stacking faults, while, in the case of the LMO samples, the white arrows show disorder within the honeycomb layers. The [010] HAADF-STEM images confirm for both samples the O3-type stacking, where the inset shows the monoclinic unit cell.

As the Z number for manganese and titanium is quite similar, those elements are difficult to be distinguished based on HAADF-STEM or Rietveld refinement of PXRD data. Characterization by  $^7\text{Li}$  magic angle spinning (MAS) nuclear magnetic resonance (NMR) spectroscopy is presented below, in order to indirectly probe the  $\text{Mn}^{4+}$  and  $\text{Ti}^{4+}$  distribution in the honeycomb layers.

The  $\text{Mn}^{4+}$  and  $\text{Ti}^{4+}$  distribution within the honeycomb layer is indirectly investigated by probing the Li environments for the LMO, LMTO-1 and LMTO-2 pristine materials by  $^7\text{Li}$  magic angle spinning (MAS) nuclear magnetic resonance (NMR) spectroscopy. Three inequivalent Li environments can be distinguished for the LMO material, with Wyckoff positions  $2c$  and  $4h$  in the Li layer and  $2b$  in the  $\text{LM}_2$  layer.<sup>47</sup> In agreement, three different Li positions are observed in the NMR spectrum (**Figure 5**). The peak at 1676 ppm is attributed to Li  $2b$  site, while the partially overlapping peaks at 851 ppm and 836 ppm can be ascribed to respectively Li at  $2c$  and  $4h$  sites. The peak around 0.15 ppm can be attributed to impurities from a diamagnetic lithium salt. Despite the same isotropic shifts for the LMTO-1 and LMTO-2 samples, the more asymmetric spinning sidebands for LMTO-1 as compared to LMTO-2 indicate a different local geometry. Grey *et al.*<sup>48,49</sup> demonstrated a model to rationalize peak shifts caused by paramagnetic Fermi contact interaction between Li and octahedrally coordinated paramagnetic metals in lithium metal oxides. The authors reported that the overall chemical shift can be deconvoluted in the contributions of each individual Li-O-Mn interaction. Those individual contributions could result in a positive or negative shift. The large chemical shift of Li in the  $2b$  position for  $\text{Li}_2\text{MnO}_3$  finds its origin in the 6  $\text{Mn}^{4+}$  cations in its first coordination shell with Li-O-Mn bond angles close to  $90^\circ$  and resulting in a delocalization of spin density due to an overlap between half-filled  $t_{2g}^*$  orbitals and empty  $\pi^*$  and Li 2s orbitals.

The absence of a peak in the 1500-1700 ppm region for both LMTO-1 and LMTO-2 samples, containing diamagnetic  $\text{Ti}^{4+}$ , would indicate a homogeneous  $\text{Mn}^{4+}$  and  $\text{Ti}^{4+}$  distribution. In the ideal  $\text{Li}_2\text{MnO}_3$  monoclinic structure, namely only one inequivalent M position ( $4g$ , in Wyckoff notation) can be distinguished. When  $\text{Li}^+$  is exclusively coordinated by diamagnetic cations, this results in a chemical shift close to zero for layered Li oxides<sup>50,51,52</sup>. Increasing the amount of  $\text{Li}^+\text{-O}^{2-}\text{-M}^{x+}$  (at  $180^\circ$  or  $90^\circ$ ) configurations in the first or second coordination sphere of  $\text{Li}^+$ , whereby  $\text{M}^{x+}$  is paramagnetic, would result in a progressive downfield shift as nuclear-spin couplings are additive.<sup>52</sup>

The absence of a peak in the 1500–1700 ppm range for both the LMTO-1 and LMTO-2 samples cannot be explained by the absence of lithium in the transition metal layer as the HAADF-STEM and SAED analysis presented earlier pointed out that the Li-M honeycomb ordering has been maintained for those samples. This implies that a reduction of the number of neighbouring  $\text{Mn}^{4+}$  cations, caused by antisite disorder in the honeycomb layer, can be excluded, as it would result in a decrease of the chemical shift of Li in the honeycomb layer.

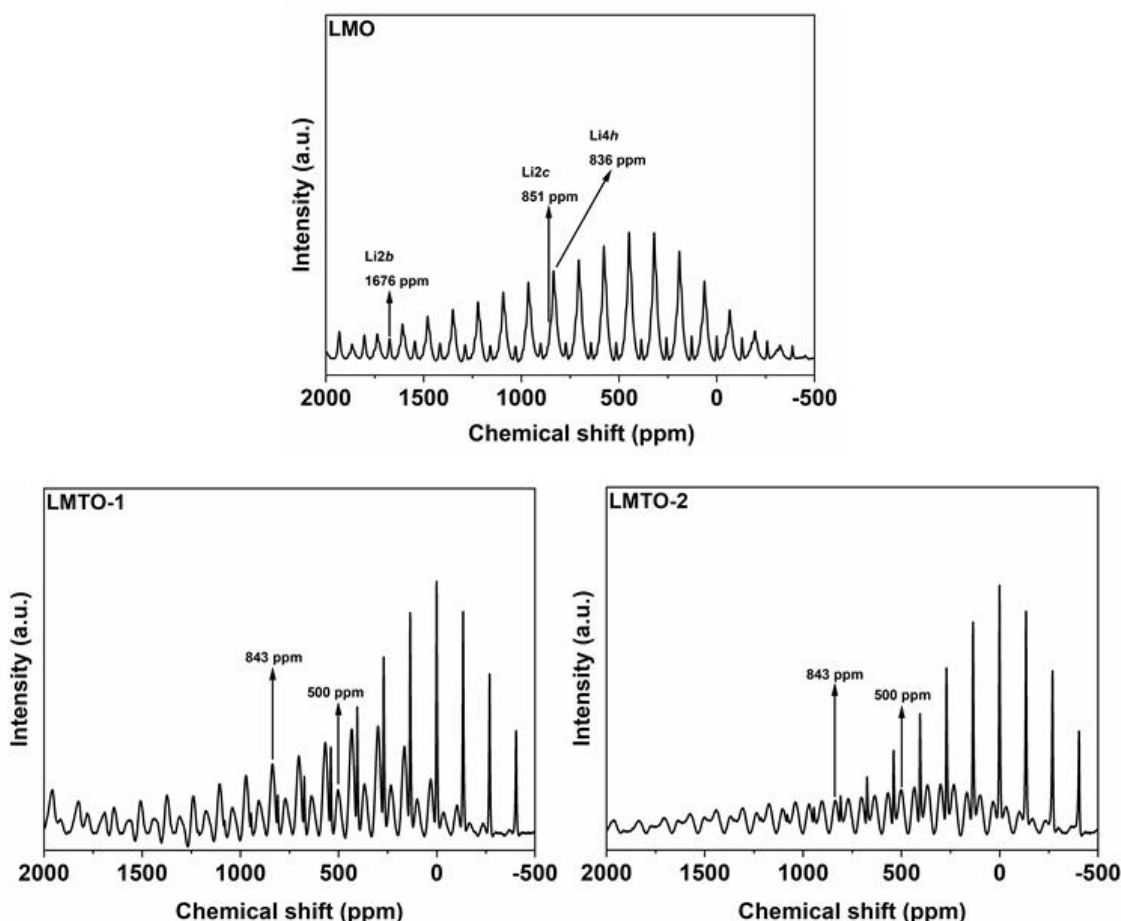


**Figure 5.**  $^7\text{Li}$  MAS NMR spectra of LMO (top), LMTO-1 (bottom, left) and LMTO-2 (bottom, right). Peaks are indicated by arrows. The corresponding Wyckoff positions for the LMO sample have been depicted. The peak around 0.15 ppm is a diamagnetic lithium salt impurity. All other signals are spinning side bands of the isotropic peaks.

## Anionic redox chemistry in $\text{Li}_2\text{Mn}_{1-x}\text{Ti}_x\text{O}_3$ : a combined theoretical and experimental approach

### *DFT study: Static calculations*

The in-depth structural study presented in the previous section confirms that the structure and  $C2/m$  symmetry are maintained up to a  $\text{Ti}^{4+}$  substitution degree of at least  $x=0.2$  in  $\text{Li}_2\text{Mn}_{1-x}\text{Ti}_x\text{O}_3$ . In addition,  $\text{Ti}^{4+}$  is indicated by  $^7\text{Li}$  MAS NMR to be randomly distributed on Mn sites in the  $\text{LM}_2$  layer. These results validated the pristine structures used for our DFT calculations assessing O-O dimer formation presented in this section, including replacing  $\text{Mn}^{4+}$  by  $\text{Ti}^{4+}$  and



assuming a random distribution of  $\text{Ti}^{4+}$ . For both the  $x=0.1$  and  $0.2$  concentration, 5 symmetry-unique structures were considered.

Firstly, the electronic properties of the  $\text{Li}_2\text{Mn}_{1-x}\text{Ti}_x\text{O}_3$  structures before delithiation were calculated. **Figure 6** shows the density of states (DOS) of the LMO and as an example for  $\text{Ti}^{4+}$ -substituted structures, the DOS of LMTO-2. As seen in these figures, the valence band of the total DOS is mainly occupied by the O states, and most of the Mn states contribute to the conduction bands. When the Mn atoms are substituted by Ti atoms, the new states shown by green color are created at the conduction band. These states come from the Ti 3d orbitals. This figure also shows that Ti orbitals have no significant contribution to the valence band.

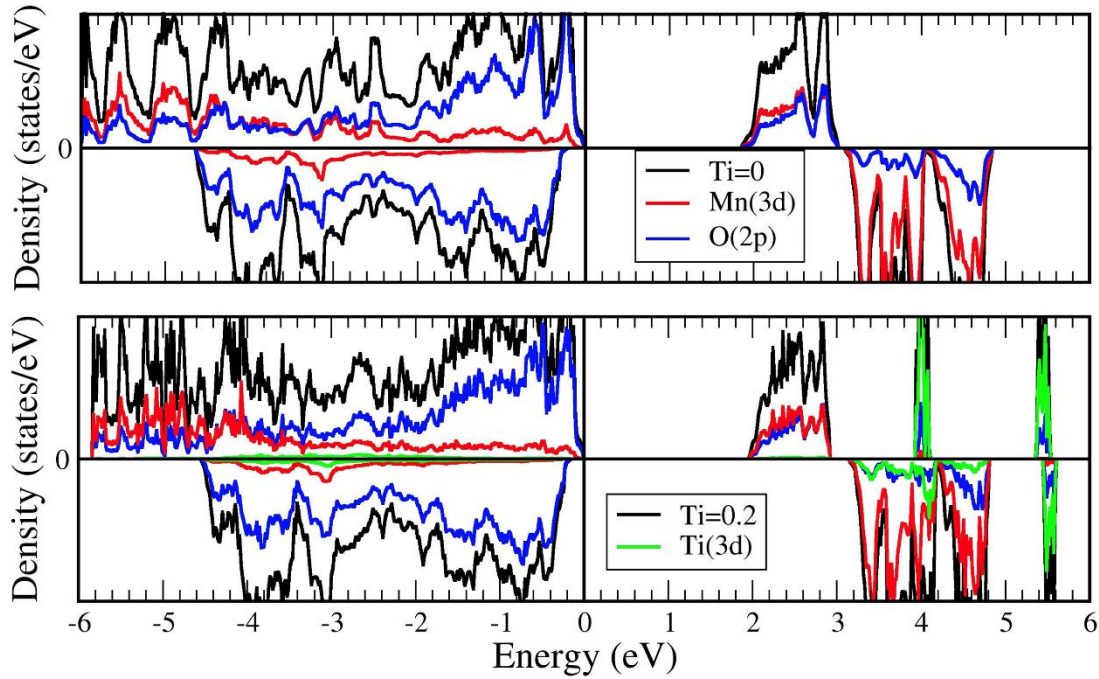


**Figure 6.** Density of states (DOS) of (up) LMO and (bottom) LMTO-2. In these figures, black is total (DOS), red, blue and green are partial DOSs of Mn, O and Ti atoms, respectively. The Fermi level is set to 0 eV. Here, positive and negative DOS values represent spin up/down electrons, respectively.

In order to study the O-O dimer formation in the Ti-substituted  $\text{Li}_2\text{MnO}_3$ , the 75% delithiated structure is considered,  $\text{Li}_{0.5}\text{Mn}_{1-x}\text{Ti}_x\text{O}_3$ . It was shown<sup>53</sup> that during the first stage of the delithiation that corresponds to 0-12.5% Li atom removal, the Li ions are only removed from the Li layer. In the next step (12.5-25%), Li ions in the mixed Li-Mn ( $\text{LM}_2$ ) layer are removed. For the (25-37.5%) delithiation stage, Li removal occurs in the Li layer, and during 37.5-50% delithiation Li ions are extracted from the  $\text{LM}_2$  layer. At this stage, all Li atoms in the  $\text{LM}_2$  layer have been removed. For further delithiation, Li ions can only be removed from the Li layer. Because stacking changes were not observed in the experiment, calculations were performed for the O3-stacking structure. In order to stay in O3-stacking, the Li atoms can only be removed from the  $4h$  positions at the Li layer. Hence, in order to obtain the 75% delithiated structures, all Li atoms from the  $\text{LM}_2$  layer must be removed as well as the Li atoms at the  $4h$  positions in the Li layer.

When Li atoms are removed from the structure, changes in the magnetic moments of the atoms were observed (**Table 3**). While the magnetic moments of the oxygen atoms are around 0 for  $\text{Li}_2\text{Mn}_{1-x}\text{Ti}_x\text{O}_3$ , their magnetic moments are around  $0.44 \mu_B$  after delithiation. On the other hand, the magnetic moments of the Mn atoms do not change significantly during the delithiation process, and are equal to  $3.03 \mu_B$ . These magnetic moments of the Mn atoms correspond to a +4 oxidation state. The magnetic moment of the Ti atoms changed from 0.03 to  $0.15 \mu_B$ . Despite this change in the magnetic moment of Ti, charge analysis showed that the oxidation state of the Ti is still +4 after removing the Li atoms.

**Table 3.** Calculated magnetic moments of Mn, O and Ti atoms in  $\text{Li}_2\text{Mn}_{1-x}\text{Ti}_x\text{O}_3$  and  $\text{Li}_{0.5}\text{Mn}_{1-x}\text{Ti}_x\text{O}_3$ . Here, the magnetic moments for  $x=0.2$  are the average of the different Ti configurations.

	in unit $\mu_B$	$\text{Li}_2\text{Mn}_{1-x}\text{Ti}_x\text{O}_3$	$\text{Li}_{0.5}\text{Mn}_{1-x}\text{Ti}_x\text{O}_3$
<b>x=0</b>	$\mu(\text{Mn})$	3.110	3.032
	$\mu(\text{O})$	0.001	0.440
<b>x=0.2</b>	$\mu(\text{Mn})$	3.100	3.020
	$\mu(\text{O})$	0.030	0.430
	$\mu(\text{Ti})$	0.030	0.150

In the Supporting Information, **Figure S12** shows the bond analysis for delithiated LMTO-2 structures. Different from LMO, LMTO-05 and LMTO-1, a spontaneously formed O-O dimer was observed in LMTO-2. This oxygen dimer has an interatomic distance of approximately 1.2 Å which corresponds to an  $\text{O}_2$  molecule.

#### *Electrochemical characterization (galvanostatic cycling)*

The LMO and LMTO-2 samples are galvanostatically cycled for 50 cycles at C/10 subsequent to two formation cycles at C/20 in the voltage interval from 2.0 V to 4.8 V vs.  $\text{Li}^+/\text{Li}$ . All tests have been repeated multiple times to estimate the reproducibility. Representative charge/discharge curves are depicted in **Figure 7**.



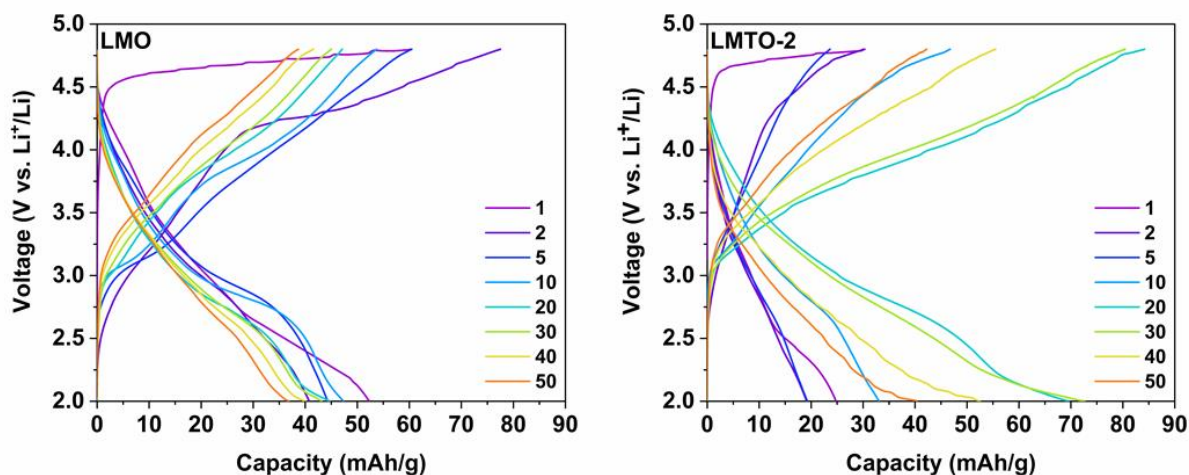


**Figure 7.** Representative charge/discharge curves (cycle number is given in the legend) in the 2.0 V–4.8 V vs.  $\text{Li}^+/\text{Li}$  voltage window for LMO (left) and LMTO-2 (right).

The  $\text{Mn}^{3+}/\text{Mn}^{4+}$  redox couple in spinel structured  $\text{LiMn}_2\text{O}_4$  is situated between below 4.5 V vs.  $\text{Li}^+/\text{Li}$ .<sup>11</sup> The very low capacity delivered by both samples within this voltage region during the first charging step indicates that manganese is present as  $\text{Mn}^{4+}$ . The shape of the initial charging step of the LMTO-2 sample is comparable to the one of LMO, indicating that upon the substitution of titanium for manganese, Mn remains in a 4+ oxidation state. This is confirmed by the absence of any spinel-type structure in the HAADF-STEM images and SAED patterns for the pristine sample as discussed earlier. However, the capacity attributed to the potential plateau at around 4.5 V is significantly larger for LMO as compared to LMTO-2. This potential plateau can most certainly be attributed to oxygen release by the active cathode material, resulting in structural degradation.<sup>54</sup> This is demonstrated by the low Coulombic efficiency for the first cycle for both samples in **Figure 8**. In **Figure 8**, the discharge capacity and Coulombic efficiency versus charge/discharge cycle number have been plotted for both LMO and LMTO-2. Cathode electrolyte interphase (CEI) formation via the oxidation of the electrolyte is also likely to occur at potentials as high as 4.5 V vs.  $\text{Li}^+/\text{Li}$ . However, as the CEI is only expected to be well passivating at potentials above 4.8 V vs.  $\text{Li}^+/\text{Li}$ , no predominant effect on the electrochemical performance is expected.<sup>55</sup>

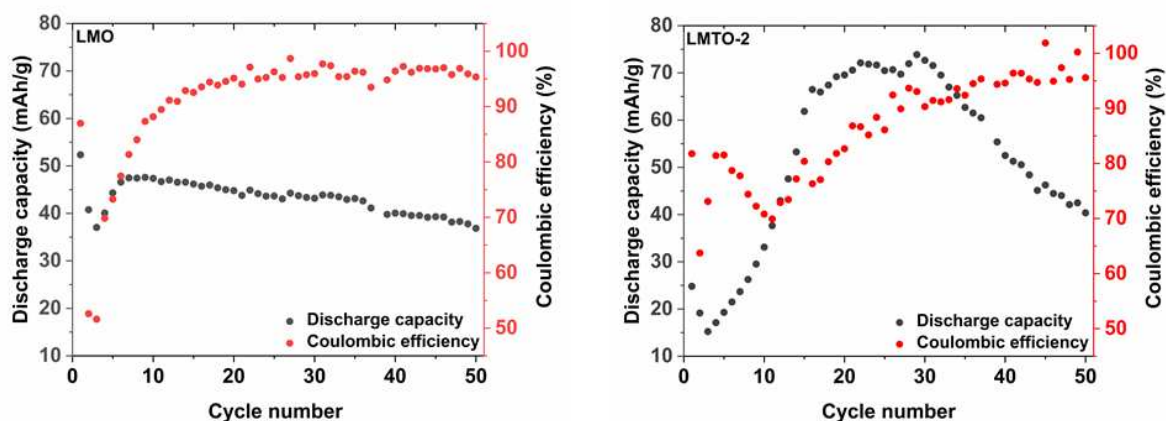


**Figure 8.** Discharge capacity and Coulombic efficiency vs. cycle number for respectively LMO (left) and LMTO-2 (right).

Retarding the anionic redox is correlated with the activation potential for anionic redox. As visible in **Figure 7**, the initial (charging step 1<sup>st</sup> cycle) Li extraction potential is shifted to a higher voltage upon Ti<sup>4+</sup> substitution. This is in agreement with the DFT calculated Li extraction potentials (4.58 V for Li<sub>0.5</sub>MnO<sub>3</sub>, 4.61 V for Li<sub>0.5</sub>Mn<sub>0.8</sub>Ti<sub>0.2</sub>O<sub>3</sub>) based on the equation 1<sup>56</sup> below. The corresponding plot depicting the lithium extraction potential vs. the Ti<sup>4+</sup> substitution degree for Li<sub>0.5</sub>Mn<sub>1-x</sub>Ti<sub>x</sub>O<sub>3</sub> is given in the Supporting Information (**Figure S13**).

$$V(\gamma) = - \frac{E(\text{Li}_2\text{Mn}_{1-x}\text{Ti}_x\text{O}_3) - E(\text{Li}_\gamma\text{Mn}_{1-x}\text{Ti}_x\text{O}_3) - (2-\gamma)E(\text{Li})}{(2-\gamma)e} \quad (1)$$

Hereby, the first and the second terms of the numerator represent the total energy of Li<sub>2</sub>Mn<sub>1-x</sub>Ti<sub>x</sub>O<sub>3</sub> and Li<sub>0.5</sub>Mn<sub>1-x</sub>Ti<sub>x</sub>O<sub>3</sub>, respectively, and E(Li) is the total energy of the metallic body-centered cubic (bcc) Li structure.

The discharge capacities for LMTO-2 (**Figure 8**) are lower for the five initial charge/discharge cycles as compared to LMO. Hereafter, however, until cycle number 30 the capacity of LMTO-2 increases to ~70 mAh/g being significantly higher than that for LMO. This strongly hints at an enhanced activation of the Mn<sup>3+</sup>/Mn<sup>4+</sup> redox couple for the LMTO-2 sample during those charge/discharge cycles. It has namely been reported for related materials that Ti<sup>4+</sup> is redox inactive within the considered potential window<sup>57</sup>. Between cycle number 30 and number 50 the discharge capacity for LMTO-2 gradually decreases to about the same value for LMO, around 40 mAh/g. The reproducibility of the peculiar electrochemical behaviour of LMTO-2 is confirmed by the discharge capacity averaged over three coin cells, presented in the Supporting Information **Figure S14** together with the standard deviation. The discharge capacity of LMO after the initial charge/discharge cycles deteriorates more steadily, showing a very gradual decay upon increasing cycle number. After reaching a minimum around 50% at cycle number 3, the Coulombic efficiency for the LMO sample reaches a plateau around cycle number 15, with efficiency exceeding 95%.

For the LMTO-2 sample, a different trend has been observed. On the contrary to LMO, a faster increase in Coulombic efficiency after the initial two charge/discharge cycles is observed, followed by a drop in efficiency reaching a minimum around 70% at cycle number 10. Afterwards a steady increase of the Coulombic efficiency till about 96% for the final cycle is obtained.

In order to have a closer look at the preliminary findings deduced from the capacity vs. voltage curves, the corresponding differential capacity (dQ/dV vs. V) plots are presented in **Figure 9**.

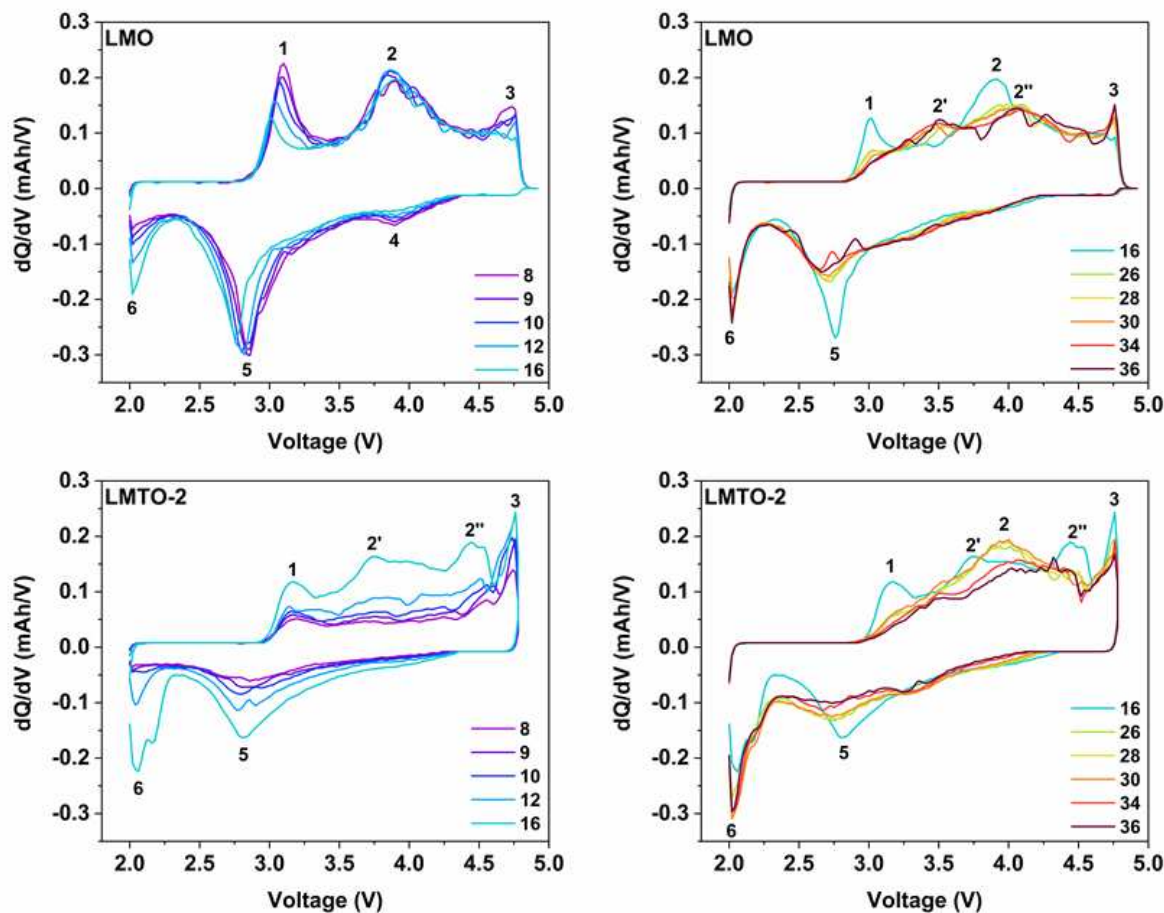


**Figure 9.** Differential capacity ( $dQ/dV$  vs.  $V$ ) plots derived from selected charge/discharge curves for LMO (top) and LMTO-2 (bottom).

Oxidation peak **1** is attributed to the  $Mn^{3+}/Mn^{4+}$  redox couple. Its shift from higher potentials to lower potentials upon increasing cycle number for LMO originates from the gradual conversion of the initial layered structure to a layered/spinel-type structure<sup>58</sup>, characteristic for extended galvanostatic cycling of the (anion deficient)  $Li_2MnO_3$ -type structure. The shifted redox couple is attributed to  $Li^+$  (de)intercalation into the spinel's 16c octahedral sites<sup>7,59,60</sup>. The gradual increase of the area of oxidation peak **1** for LMTO-2, when comparing cycle numbers 8 to 16, agrees with a delayed activation of the LMTO-2. Correspondingly, the area of the main reduction peak **5**, situated at around 2.7 V vs.  $Li^+/Li$ , shows a faster decay for the LMTO-2 sample at cycle numbers above about 16 preceded by a delayed increase at cycle numbers until about 16.

Simultaneously, reduction peak **6** becomes more prominent. This peak, situated around 2.05 V, can be ascribed to the  $Mn^{4+}/Mn^{3+}$  redox couple in the spinel-type.<sup>7,61</sup> The structural degradation to a spinel-type structure, with  $Fd-3m$  symmetry, is evidenced by the SAED patterns recorded after 50 charge/discharge cycles presented in Supporting Information **Figure S15** and **Figure S17** (see further).

The broad band of oxidation peaks **2'**, **2** and **2''** in the 3.55 - 4.5 V interval is probably associated with  $Li^+$  extraction from a (more delithiated) spinel-type structure<sup>62</sup>, and as such supports the gradual conversion of both samples to a spinel-type structure.

The gradual conversion from the initial layered structure to a spinel-type and eventually a rock-salt type structure is strongly associated with anionic redox chemistry of the oxygen sublattice, as demonstrated by comparing the LMO and LMTO-2 samples. This is confirmed by oxidation peak **3** at around 4.75 V vs.  $\text{Li}^+/\text{Li}$ , associated with anionic redox chemistry, being more pronounced for the LMTO-2 sample. The shoulder to peak **5**, between 3.0 and 3.5 V vs.  $\text{Li}^+/\text{Li}$  most probably corresponds to oxygen reduction<sup>63</sup> and it particularly pronounced for LMTO-2 for cycle numbers up to about 16. This implies that  $\text{Ti}^{4+}$  substitution improves the reversibility of the anionic redox, which is in line with the lower activity of the  $\text{Mn}^{3+}/\text{Mn}^{4+}$  redox couple, especially at cycle number  $\leq 16$ .

### *Structural characterization after galvanostatic cycling*

The average amount of amorphous phase present in the structure is significantly higher for the cycled LMTO-2 sample than for the cycled LMO sample, which agrees with the electrochemical results presented before. This is revealed by the HAADF-STEM images of the LMO and LMTO-2 (resp. **Figure 10** and **Figure 11**) materials after 50 cycles and in the discharged state. The majority of the particles of the cycled LMO sample are still crystalline with only an amorphous surface layer, of which the thickness varies between 0-10 nm, while in the case of the cycled LMTO-2, the amorphicity varies from a few nanometers surface layer to entirely amorphous particles. Since particles that are completely amorphous do not show any reflections in SAED, while mapping the sample in reciprocal space, these particles will go unnoticed.

The structural degradation to a spinel-type structure, with  $Fd-3m$  symmetry, and a rock-salt-type structure, possessing  $Fm-3m$  symmetry, is shown by the SAED patterns added to the Supporting Information. For the cycled LMO sample, the SAED pattern (**Figure S15**) reveals that the structural degradation does not evolve homogeneously within a single particle. Many reflections in the SAED pattern are broad and slightly diffuse, which points towards a reduced crystallinity. An inhomogeneous structural degradation is also observed for the LMTO-2 sample. By comparing the relative intensities between the reflections, the SAED patterns of LMTO-2 (**Figure S17**) allowed to derive the simultaneous presence of spinel  $Fd-3m$  and rock-salt  $Fm-3m$  type structures within some particles. The broad slightly diffuse reflections for LMTO-2 also here indicate a reduced crystallinity. On the other hand, the top SAED patterns in **Figure S17** demonstrate a particle whose structure fully retained its pristine structure. Such a particle most likely did not participate in the charge/discharge cycling because of, most probably, a poor contact with the current collector.

Due to the structure degradation, the signal-to-noise ratio of the HAADF-STEM images obtained from the cycled LMO and LMTO-2 samples is too low to see single M atoms at the tetrahedral voids or in octahedral Li positions. Therefore, to investigate the transition metal migration upon cycling, line profiles (**Figure S10**) were taken perpendicular to the layers in the HAADF-STEM images of **Figure 10** and **Figure 11**, from the areas indicated in **Figure S9**. The relative intensity of the different peaks in the line profile provides statistical information

about the transition metal migration as the peak intensities are a sum over different equivalent positions as shown in **Figure S9**. The line profiles were taken from particles still having a layered structure, with at the most an amorphous surface layer. Considerable M migration to the Li layers during galvanostatic cycling has occurred during cycling for both the LMO and LMTO-2 samples. In the case of the LMTO-2 sample, the relative intensity of the peaks corresponding to the overlapping peaks of the tetrahedral and O-positions is significantly higher as compared to those same peaks for the pristine sample, indicating that the M cations have migrated towards the tetrahedral positions during galvanostatic cycling. For LMO, the line profile of the cycled sample shows no significant differences from the pristine sample, and therefore, based on the HAADF-STEM images, we can only conclude that less or almost no M cations have migrated towards the tetrahedral positions. Both  $\text{Mn}^{3+}$  and  $\text{Mn}^{4+}$  do not like to occupy positions with tetrahedral coordination unlike  $\text{Ti}^{4+}$ , which can explain the higher amount of M occupying tetrahedral positions in the LMTO-2 sample.

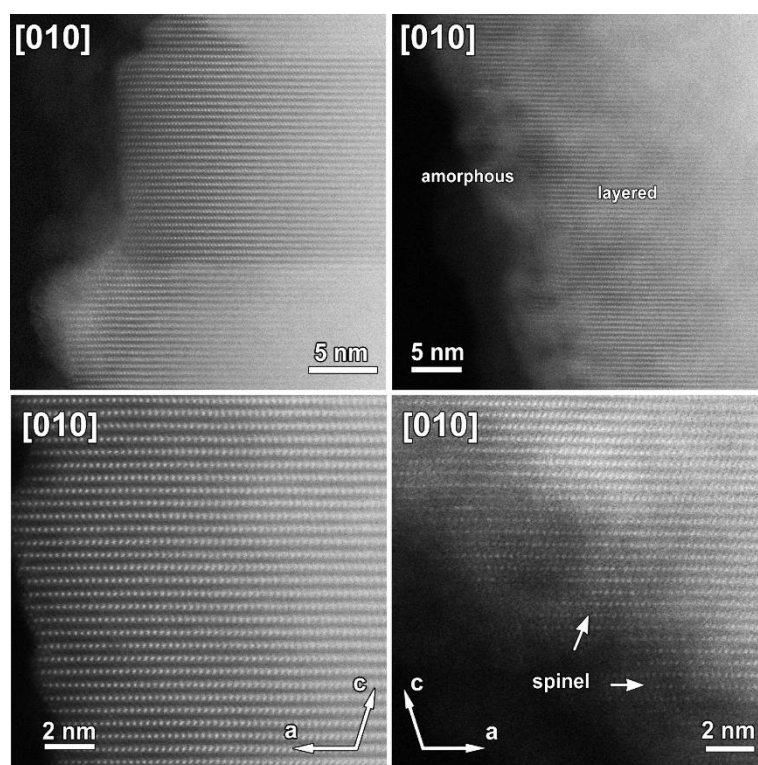


**Figure 10.** Representative HAADF-STEM images taken from the cycled LMO sample. Left: particles that remained mainly layered, right: particles with considerable structural degradation at the surface, either amorphous or spinel.

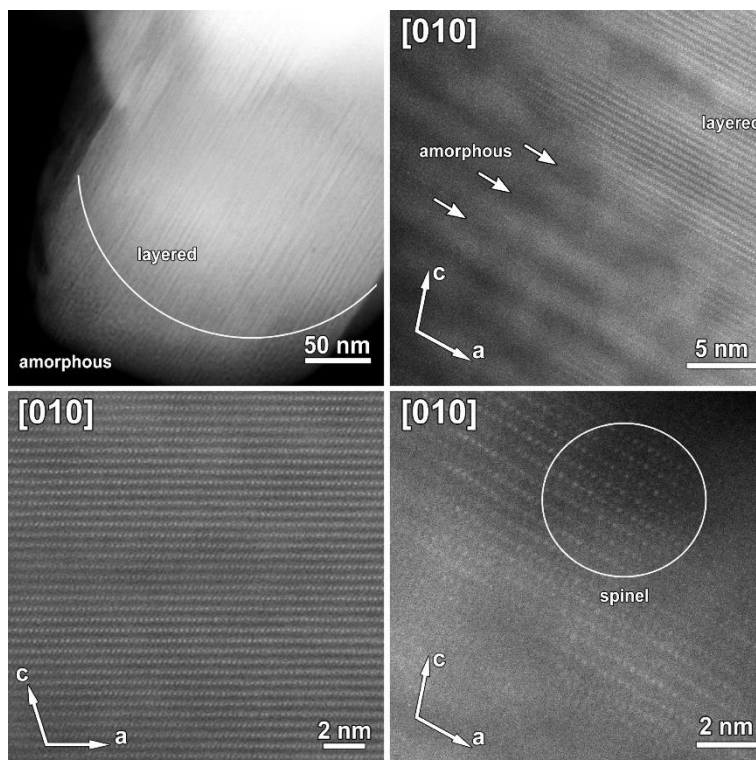


**Figure 11.** Representative HAADF-STEM images taken from the cycled LMTO-2 sample. The bulk of the particles is mainly layered where the pronounced stripes correspond to amorphous regions (left side images), while the surface is mainly amorphous with some areas corresponding to a spinel-like structure (right side images). The darker regions are amorphous.

#### *DFT study: Molecular dynamics simulations*

From the previous sections, we conclude that  $\text{Ti}^{4+}$  for  $\text{Mn}^{4+}$  substitution ( $x=0.2$  in  $\text{Li}_2\text{Mn}_{1-x}\text{Ti}_x\text{O}_3$ ) is a viable strategy to initially retard the activation of the anionic redox towards irreversible oxygen release. Our static DFT calculations presented before pointed towards O-O dimer formation facilitated by  $\text{Ti}^{4+}$ . Because the Ti-O bond is stronger than the Mn-O bond, it is expected that Ti substitution can stabilize the O-O dimers hampering excessive oxygen release, which could explain the lower activation towards irreversible oxygen release in the initial charging step for LMTO-2 as compared to LMO. However, remarkably, upon extended cycling a more pronounced anionic redox contribution to the total capacity is observed for LMTO-2 as compared to LMO. The associated structural degradations are related to the migration of Mn to the Li layer, which are believed to be responsible for voltage fade in this type of Li-rich oxide cathode materials.

In order to better understand the influence of the Ti substitution on the local structural stability we performed ab initio molecular dynamics (MD) simulations for LMO, LMTO-05, LMTO-1 and LMTO-2 in which we focused on the migration of Mn and the oxygen dimer formation. As discussed in the section on the static DFT calculations, we performed these MD simulations for 5 symmetrically non-equivalent structures for LMTO-1 and LMTO-2, and the results shown in this section were obtained by taking the average over these structures. We performed our MD



simulations at 300 K and 1000 K, respectively. Hereafter, we present the results obtained for 1000 K. Some of the results for 300 K are also shown in Supporting Information **Figure S18**.

In order to study the displacement of Mn atoms in the structures, their mean square displacement (MSD) with respect to time were calculated and the results are shown in **Figure 12**. Here the MSD is obtained from the average of the displacements of all Mn atoms. As seen in Fig. 12, the MSD increases with time for all structures. But note that the MSD of Mn in LMTO-05 is clearly below the MSD in LMO, LMTO-1 and LMTO-2 up to 17 ps. Ti substitution seems indeed to stabilize the environment, but only in low concentrations.

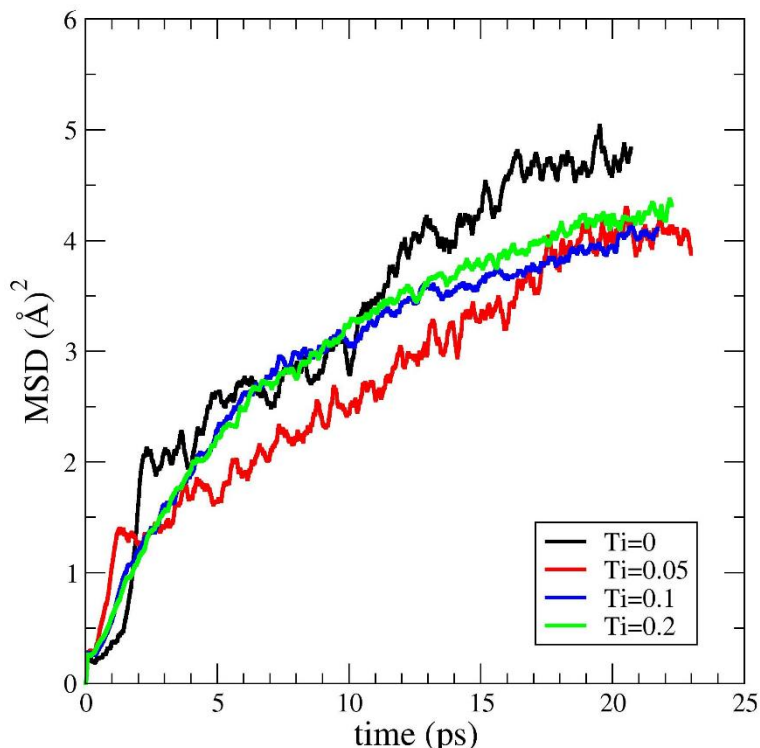


**Figure 12.** Mean square displacement (MSD) for Mn atoms with respect to the MD time step for LMO (black), LMTO-05 (red), LMTO-1 (blue) and LMTO-2 (green). For LMTO-1 and LMTO-2 structures, the results are the average of 5 different MD simulations (**Figure S24**). Here, time steps are in ps. Temperature is 1000 K.

It is known that Mn displacement is strongly related with the dynamics of the oxygen atoms<sup>64,65,66</sup> and it has been proposed that metal atom displacements can only be understood together with the oxygen dimerization<sup>67</sup>. Therefore, the oxygen dimer fraction ( $n(\text{O}_2)/n(\text{O})$ ) and the pair distribution function ( $g(r)$ ) for the oxygen atoms were also calculated as a function of time. Oxygen dimers are defined as O-O pairs having a bond length below 1.7 Å. The simulations were continued until a converged value for the dimer fraction was reached.

The O-O dimer fraction as a function of time is shown in **Figure 13**. As seen in this figure, the dimer fraction increases with respect to time for all structures. For the first 5 ps, LMTO-2 has a higher number of O-O dimers. This could be attributed to the  $\text{Ti}^{4+}\text{-O}$  bond being less

directional than its  $\text{Mn}^{4+}$ -O counterpart due to the lack of partially filled d orbitals for the former, facilitating the rotation to hybridize oxidized Li-O-Li states of two adjacent oxidized oxygens required to form  $(\text{O}_2)^{n-}$ -like species. After 15 ps, all structures have almost the same dimer fraction. The  $n(\text{O}_2)/n(\text{O})$  values for the different configurations of LMTO-1 and LMTO-2 are shown in **Figure S19**.

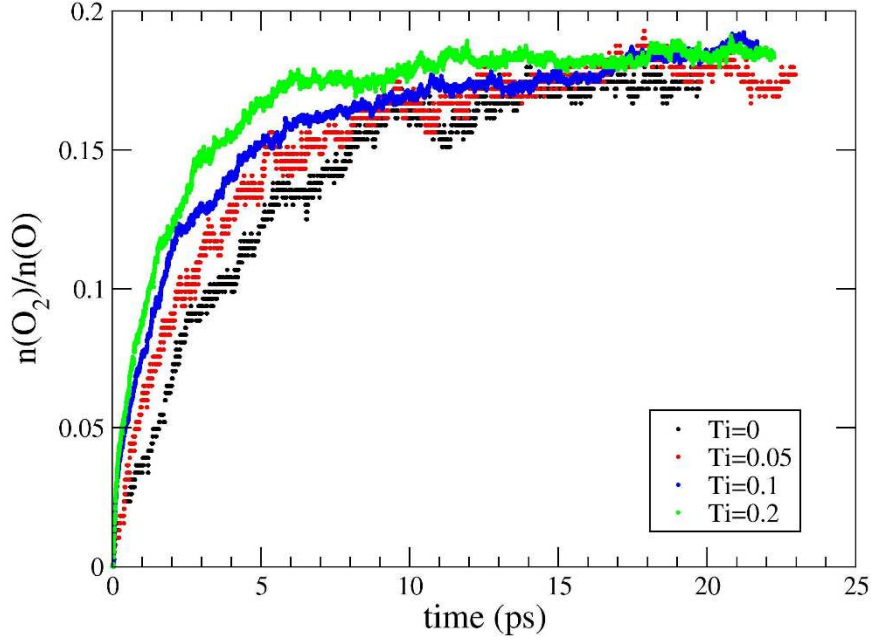


**Figure 13.** O-O dimer fraction ( $n(\text{O}_2)/n(\text{O})$ ) with respect to the number of MD time steps for LMO (black), LMTO-05 (red), LMTO-1 (blue) and LMTO-2 (green). For LMTO-1 and LMTO-2, the results are the average of 5 different MD simulations. Here, time steps are in ps.  $n(\text{O}_2)$  is the total number of dimers and  $n(\text{O})$  is the total number of oxygen atoms in the structures. Temperature is 1000 K.

In order to calculate the energy barrier for the dimer formation, we fitted the number of dimers to the following equation<sup>65</sup>

$$n_{\text{O}_2}(t) = n_0(1 - \exp(-t/t_0)) \quad (2)$$

where  $n_{\text{O}_2}$  is the number of dimers and  $n_0$  and  $t_0$  are constants. If the process at  $t=0$  has an activation energy  $E_a$  then it can be calculated from the equation

$$dn_{\text{O}_2}(t)/dt|_{t=0} = n_0/t_0 \approx 3\nu \exp(-E_a/k_bT). \quad (3)$$

In this equation,  $\nu$  is the vibrational frequency and typical values are  $10^{11} \text{ s}^{-1}$  to  $10^{13} \text{ s}^{-1}$ ,<sup>56</sup> we use  $10^{13} \text{ s}^{-1}$  in our calculations. In **Figure S20**, the fitting for LMO is shown and in **Figure S21**  $E_a$  values for all structures and for all configurations of LMTO-1 and LMTO-2 are represented. As seen in this figure, the  $E_a$  value for LMO is 0.57 eV which is very close to the calculated values for  $\text{Li}_{0.5}\text{MnO}_3$  presented in literature<sup>31,65,68</sup>. Also note that the activation energy decreases with increasing Ti concentration.



This obtained activation barrier is also the reason why it was chosen to perform the MD simulations at 1000 K, following references<sup>64,65,69</sup>. For this activation barrier, simulations at low temperatures will not show a significant dimer formation on the computational time scale (especially for LMO and LMTO-05). Our 300 K results for dimer formation shown in Supporting Information **Figure S18** illustrate this statement.

The number of formed dimers alone is not enough to understand the local stability of the structures. The O-O dimers exist in different forms that behave completely different. If the distance between the oxygen atoms is typically larger than 1.3 Å, it is observed that the dimers form peroxide or superoxide and each oxygen atom of that dimer is bonded to a metal ion. If the distance between the oxygen atoms of the dimer is less than 1.3 Å, either one of the oxygen atoms is bonded to one metal ion or they are free O<sub>2</sub> molecules. So, it is expected that structures in which a larger quantity of free O<sub>2</sub> molecules are formed, and thus more oxygen vacancies, are the least stable ones. In order to observe the time evolution of dimer bond lengths, the time-dependent pair distribution function  $g(r)$  is shown in **Figure 14**. The black line indicates the transition from O<sub>2</sub> molecules to peroxide and superoxide.

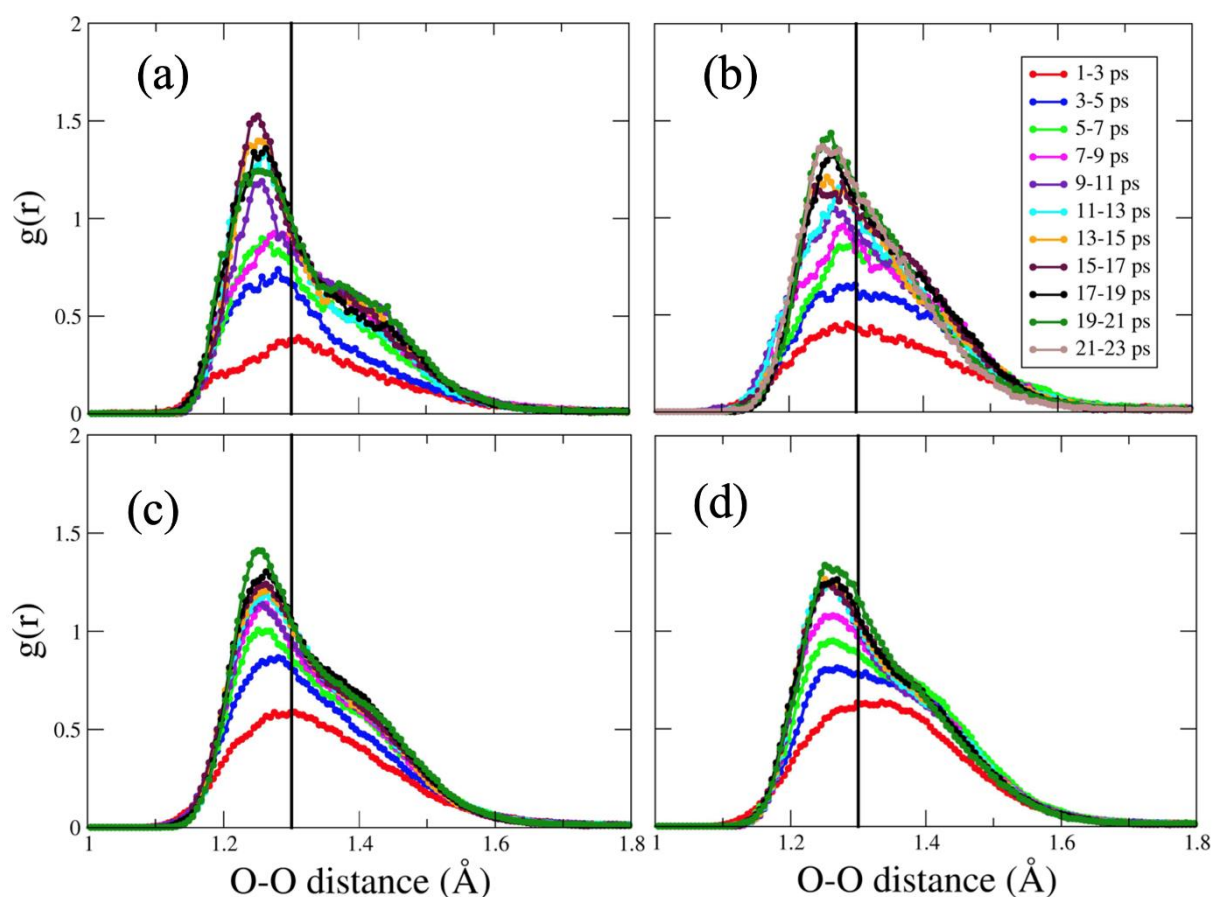


**Figure 14.** The pair distribution function  $g(r)$  with respect to O-O distance for (a) LMO, (b) LMTO-05, (c) LMTO-1 and (d) LMTO-2. Here the color lines show the time interval for the average of  $g(r)$ . For LMTO-1 and LMTO-2, pair distribution functions  $g(r)$  for each of the 5 different Ti position configurations were calculated (resp. **Figure S22** and **Figure S23**). The black line indicates the transition from O<sub>2</sub> molecules to peroxide and superoxide.

The time evolution of  $g(r)$  for LMO, LMTO-1 and LMTO-2 is similar. From the start onwards, the distribution is asymmetric, and a peak grows around 1.24 Å and thus relatively more O<sub>2</sub> molecules are formed in comparison to the peroxide and superoxide structures. The distribution for LMTO-05 evolves more symmetrically up to 17 ps, indicating that the O<sub>2</sub> formation is not dominant. This is consistent with our earlier observation that the smallest MSD for Mn was observed in LMTO-05.

We can conclude from our MD calculations that Ti substitution can indeed stabilize the local environment in LMO, but only at low substitution degrees ( $x < 0.1$ ). At larger substitution degrees, it also favors the formation of the O-O dimers to be released as O<sub>2</sub>, which reduces the stability again. The latter explains why experimentally after extended cycling significant structural degradation is observed also for LMTO-2. However, during the initial cycle(s) the activation of anionic redox towards oxygen release is retarded for LMTO-2 as compared to LMO most likely due to the lower relative Mn content and partial stabilization of the formed dimers by the stronger Ti-O bond.

## Conclusion

This work comprised an in-depth study of the influence of Ti<sup>4+</sup> substitution in Li<sub>2</sub>Mn<sub>1-x</sub>Ti<sub>x</sub>O<sub>3</sub> on crystal structure and electrochemical performance when applied as cathode material for Li-ion batteries. We showed that, up to a substitution degree of at least  $x=0.2$ , the crystal structure retained its *C2/m* symmetry with a homogeneous Mn and Ti distribution in the LM<sub>2</sub> layer. Galvanostatic cycling was performed on  $x=0$  (LMO) and  $x=0.2$  (LMTO-2) compositions. We experimentally revealed that a high Ti substitution degree retards irreversible oxygen release. However, upon extended cycling, the contribution of anionic redox to the total capacity was higher for LMTO-2 as compared to LMO, resulting in a more pronounced structural degradation for the former. This agreed with the outcome of our static DFT and MD calculations, confirming a low activation energy barrier towards O-O dimer formation and Mn migration for LMTO-2 in “charged” Li<sub>0.5</sub>Mn<sub>0.8</sub>Ti<sub>0.2</sub>O<sub>3</sub> as is also the case for the “charged” parent material. Particularly, the higher tendency for O-O dimer formation in the 5 ps timeframe for LMTO as compared to LMO, could be most likely attributed to the Ti<sup>4+</sup>-O bond being less directional than its Mn<sup>4+</sup>-O counterpart due to the lack of partially filled d orbitals for the former, facilitating the rotation to hybridize oxidized Li-O-Li states of two adjacent oxidized oxygens required to form (O<sub>2</sub>)<sup>n-</sup>-like species. It should be noted that similar oxygen release retardation has been also observed in Ru<sup>4+</sup>-doped Li-rich Ni-Mn layered oxides, but its origin appears to be intrinsically different from the role of Ti<sup>4+</sup>: Ru<sup>4+</sup> has some d-electrons on more spacious 4d-orbitals thus increasing the covalency of the metal-oxygen bonding<sup>70</sup>. Remarkably, our MD calculations pointed towards a higher structural stability upon lowering the Ti substitution degree to  $x=0.05$ . This emphasizes the importance of carefully optimizing the substitution degree to achieve the best electrochemical performance.

As a general conclusion, our study points towards the important interplay between tendency of dimer formation, dimer stabilization towards O<sub>2</sub> release, relative Mn content and dopant

concentration. Careful optimization of the latter with regard to the other important parameters is crucial to obtain a well performing cathode material.

## Supporting Information

**Structural characterization:** PXRD patterns for all samples fitted with the Le Bail method, Particle size distribution for all samples, STEM-EDX mixed elemental maps for LMTO-3 sample, Raman spectra for LMO, LMTO-1 and LMTO-2 samples, HAADF-STEM images for LMO, LMTO-1 and LMTO-2 (pristine) and LMO and LMTO-2 (cycled), line profiles for LMO, LMTO-1 and LMTO2 (pristine) and LMO and LMTO-2 (cycled), SAED patterns for LMTO-1 (pristine) and LMO and LMTO-2 (cycled), simulation of the HAADF-STEM image of the pristine structure, different calculated ED patterns that are present in the experimental SAED patterns of cycled LMO. **Electrochemical characterization:** Discharge capacity vs. cycle number for LMTO-2, averaged over three coin cells. **First-principles calculations:** O-O distance for  $\text{Li}_{0.5}\text{Mn}_{1-x}\text{Ti}_x\text{O}_3$ , Lithium extraction voltage for LMO, LMTO-05, LMTO-1 and LMTO-2, O-O dimer fraction for LMO, LMTO-05, LMTO-1 and LMTO-2 at 300 and 1000 K, activation energy ( $E_a$ ), pair distribution functions, mean square distance (MSD) of Mn atoms.

## Acknowledgements

The authors acknowledge Research Foundation Flanders (FWO Vlaanderen) project number G040116N for funding. The authors also acknowledge support by Hasselt University and the Research Foundation Flanders for the Hercules project AUHL/15/2 - GOH3816N. A.M.A acknowledges support from Russian Science Foundation (grant 20-43-01012). The computational resources and services used in this work were provided by the VSC (Flemish Supercomputer Center) and the HPC infrastructure of the University of Antwerp (CalcUA), both funded by the FWO-Vlaanderen and the Flemish Government-department EWI.

The authors are grateful to Dr Olesia M. Karakulina (UAntwerpen, EMAT) for performing the PXRD measurements. The authors wish to thank Greet Cuyvers (UHasselt, Institute for Materials Research, Analytical and Circular Chemistry) for performing microwave digestion prior to ICP-AES and ICP-AES measurements and An-Sofie Kelchtermans (UHasselt, Institute for Materials Research, DESINE) for performing ICP-AES on monometal precursors. The authors thank Dr Saeed Yari (UHasselt, Institute for Materials Research) for fruitful discussions on slurry formulation.

## References

- (1) Saubanère, M.; McCalla, E.; Tarascon, J.-M.; Doublet, M.-L. The Intriguing Question of Anionic Redox in High-Energy Density Cathodes for Li-Ion Batteries. *Energy Environ. Sci.* **2016**, *9*, 984–991. <https://doi.org/10.1039/c5ee03048j>.
- (2) Xie, Y.; Saubanère, M.; Doublet, M.-L. Requirements for Reversible Extra-Capacity in Li-Rich Layered Oxides for Li-Ion Batteries. *Energy Environ. Sci.* **2017**, *10*, 266–274. <https://doi.org/10.1039/c6ee02328b>.
- (3) Assat, G.; Tarascon, J. Fundamental Understanding and Practical Challenges of Anionic Redox Activity in Li-Ion Batteries. *Nat. Energy* **2018**, *3*, 373–386. <https://doi.org/10.1038/s41560-018-0097-0>.
- (4) Abakumov, A. M.; Fedotov, S. S.; Antipov, E. V.; Tarascon, J. M. Solid State Chemistry for Developing Better Metal-Ion Batteries. *Nat. Commun.* **2020**, *11* (1), 1–

14. <https://doi.org/10.1038/s41467-020-18736-7>.
- (5) Koga, H.; Croguennec, L.; Mannesiez, P.; Bourgeois, L.; Duttine, M.; Suard, E.; Delmas, C. Li<sub>1.20</sub>Mn<sub>0.54</sub>Co<sub>0.13</sub>Ni<sub>0.13</sub>O<sub>2</sub> with Different Particle Sizes as Attractive Positive Electrode Materials for Lithium-Ion Batteries: Insights into Their Structure. *J. Phys. Chem. C* **2012**, *116*, 13497–13506. <https://doi.org/10.1021/jp301879x>.
- (6) Bréger, J.; Jiang, M.; Dupré, N.; Meng, Y. S.; Shao-Horn, Y.; Ceder, G.; Grey, C. P. High-Resolution X-Ray Diffraction, DIFFaX, NMR and First Principles Study of Disorder in the Li<sub>2</sub>MnO<sub>3</sub>-Li[Ni<sub>1/2</sub>Mn<sub>1/2</sub>]O<sub>2</sub> Solid Solution. *J. Solid State Chem.* **2005**, *178* (9), 2575–2585. <https://doi.org/10.1016/j.jssc.2005.05.027>.
- (7) Saroha, R.; Gupta, A.; Panwar, A. K. Electrochemical Performances of Li-Rich Layered-Layered Li<sub>2</sub>MnO<sub>3</sub>-LiMnO<sub>2</sub> Solid Solutions as Cathode Material for Lithium-Ion Batteries. *J. Alloys Compd.* **2017**, *696*, 580–589. <https://doi.org/10.1016/j.jallcom.2016.11.199>.
- (8) Boulineau, A.; Croguennec, L.; Delmas, C.; Weill, F. Reinvestigation of Li<sub>2</sub>MnO<sub>3</sub> Structure : Electron Diffraction and High Resolution TEM. *Chem. Mater.* **2009**, *21*, 4216–4222. <https://doi.org/10.1021/cm900998n>.
- (9) Koyama, Y.; Tanaka, I.; Nagao, M.; Kanno, R. First-Principles Study on Lithium Removal from Li<sub>2</sub>MnO<sub>3</sub>. *J. Power Sources* **2009**, *189* (1), 798–801. <https://doi.org/10.1016/j.jpowsour.2008.07.073>.
- (10) Huang, Y.; Liu, L.; Gao, M. Molecular Dynamics Study on the Li Diffusion Mechanism and Delithiation Process of Li<sub>2</sub>MnO<sub>3</sub>. *Solid State Ionics* **2020**, *346* (September 2019), 115195. <https://doi.org/10.1016/j.ssi.2019.115195>.
- (11) Yabuuchi, N. Material Design Concept of Lithium-Excess Electrode Materials with Rocksalt-Related Structures for Rechargeable Non-Aqueous Batteries. *Chem. Rec.* **2019**, *19* (4), 690–707. <https://doi.org/10.1002/tcr.201800089>.
- (12) Seymour, I. D.; Chakraborty, S.; Middlemiss, D. S.; Wales, D. J.; Grey, C. P. Mapping Structural Changes in Electrode Materials: Application of the Hybrid Eigenvector-Following Density Functional Theory (DFT) Method to Layered Li<sub>0.5</sub>MnO<sub>2</sub>. *Chem. Mater.* **2015**, *27* (16), 5550–5561. <https://doi.org/10.1021/acs.chemmater.5b01674>.
- (13) Wang, R. Atomic Structure of Li<sub>2</sub>MnO<sub>3</sub> after Partial Delithiation and Re-Lithiation. *Adv. Energy Mat.* **2013**, *3*, 1358–1367.
- (14) Phillips, P. J.; Bareño, J.; Li, Y.; Abraham, D. P.; Klie, R. F. On the Localized Nature of the Structural Transformations of Li<sub>2</sub>MnO<sub>3</sub> Following Electrochemical Cycling. *Adv. Energy Mater.* **2015**, *5* (23), 1–12. <https://doi.org/10.1002/aenm.201501252>.
- (15) Amalraj, S. F.; Burlaka, L.; Julien, C. M.; Mauger, A.; Kovacheva, D.; Talianker, M.; Markovsky, B.; Aurbach, D. Phase Transitions in Li<sub>2</sub>MnO<sub>3</sub> Electrodes at Various States-of-Charge. *Electrochim. Acta* **2014**, *123*, 395–404. <https://doi.org/10.1016/j.electacta.2014.01.051>.
- (16) Ruther, R. E.; Dixit, H.; Pezeshki, A. M.; Sacci, R. L.; Cooper, V. R.; Nanda, J.; Veith, G. M. Correlating Local Structure with Electrochemical Activity in Li<sub>2</sub>MnO<sub>3</sub>. *J. Phys. Chem. C* **2015**, *119* (32), 18022–18029. <https://doi.org/10.1021/acs.jpcc.5b03900>.
- (17) Yahia, M. Ben; Vergent, J.; Saubanère, M.; Doublet, M.-L. Unified Picture of Anionic Redox in Li/Na-Ion Batteries. *Nat. Mater.* **2019**, *18*, 496–502. <https://doi.org/10.1038/s41563-019-0318-3>.
- (18) Feng, X.; Gao, Y.; Ben, L.; Yang, Z.; Wang, Z.; Chen, L. Enhanced Electrochemical Performance of Ti-Doped Li<sub>1.2</sub>Mn<sub>0.54</sub>Co<sub>0.13</sub>Ni<sub>0.13</sub>O<sub>2</sub> for Lithium-Ion Batteries. *J. Power Sources* **2016**, *317*, 74–80. <https://doi.org/10.1016/j.jpowsour.2016.03.101>.
- (19) Seo, D.-H.; Lee, J.; Urban, A.; Malik, R.; Kang, S.; Ceder, G. The Structural and Chemical Origin of the Oxygen Redox Activity in Layered and Cation-Disordered Li-Excess Cathode Materials. *Nat. Chem.* **2016**, *8* (7), 692–697.

- <https://doi.org/10.1038/nchem.2524>.
- (20) Liu, S.; Liu, Z.; Shen, X.; Wang, X.; Liao, S. C.; Yu, R.; Wang, Z.; Hu, Z.; Chen, C. Te; Yu, X.; Yang, X.; Chen, L. Li–Ti Cation Mixing Enhanced Structural and Performance Stability of Li-Rich Layered Oxide. *Adv. Energy Mater.* **2019**, 9 (32), 1–10. <https://doi.org/10.1002/aenm.201901530>.
  - (21) Hardy, A.; D’Haen, J.; Van Bael, M. K.; Mullens, J. An Aqueous Solution-Gel Citratoperoxo-Ti(IV) Precursor: Synthesis, Gelation, Thermo-Oxidative Decomposition and Oxide Crystallization. *J. Sol-Gel Sci. Technol.* **2007**, 44 (1), 65–74. <https://doi.org/10.1007/s10971-007-1601-3>.
  - (22) Petříček, V.; Dušek, M.; Palatinus, L. Crystallographic Computing System JANA2006 : General Features. *Z. Krist.* **2014**, 229 (5), 345–352. <https://doi.org/10.1515/zkri-2014-1737>.
  - (23) Wojdyr, M. Fityk: A General-Purpose Peak Fitting Program. *J. Appl. Crystallogr.* **2010**, 43 (5 PART 1), 1126–1128. <https://doi.org/10.1107/S0021889810030499>.
  - (24) Hohenberg, P.; Kohn, W. Inhomogeneous Electron Gas. *Phys. Rev.* **1964**, 136, B864–871. <https://doi.org/10.1007/BF01198136>.
  - (25) Kohn, W.; Sham, L. Self-Consistent Equations Including Exchange and Correlation Effects. *Phys. Rev.* **1965**, 140, A1133–A1138.
  - (26) Perdew, J. P.; Burke, K.; Ernzerhof, M. Generalized Gradient Approximation Made Simple. *Phys. Rev. Lett.* **1996**, 77 (18), 3865–3868. <https://doi.org/10.1103/PhysRevLett.77.3865>.
  - (27) Kresse, G.; Hafner, J. Ab Initio Molecular Dynamics for Liquid Metals. *Phys. Rev. B* **1993**, 47 (1), 558–561. <https://doi.org/10.1103/PhysRevB.47.558>.
  - (28) Kresse, G.; Hafner, J. Norm-Conserving and Ultrasoft Pseudopotentials for First-Row and Transition Elements. *J. Phys. Condens. Matter* **1994**, 6, 8245–8257. <https://doi.org/10.1088/0953-8984/6/40/015>.
  - (29) Kresse, G.; Furthmüller, J. Efficiency of Ab-Initio Total Energy Calculations for Metals and Semiconductors Using a Plane-Wave Basis Set. *Comput. Mater. Sci.* **1996**, 6, 15–50.
  - (30) Kresse, G.; Furthmüller, J. Efficient Iterative Schemes for Ab Initio Total-Energy Calculations Using a Plane-Wave Basis Set. *Phys. Rev. B* **1996**, 54, 1169–1186. <https://doi.org/10.1021/acs.jpca.0c01375>.
  - (31) Bercx, M.; Slap, L.; Partoens, B.; Lamoen, D. First-Principles Investigation of the Stability of the Oxygen Framework of Li-Rich Battery Cathodes. *MRS Adv.* **2019**, 4, 813–820. <https://doi.org/10.1557/adv.201>.
  - (32) Morgan, B. J.; Watson, G. W. A Density Functional Theory + u Study of Oxygen Vacancy Formation at the (110), (100), (101), and (001) Surfaces of Rutile TiO<sub>2</sub>. *J. Phys. Chem. C* **2009**, 113, 7322–7328. <https://doi.org/10.1021/jp811288n>.
  - (33) Bocquet, A.; Mizokawa, T.; Morikawa, K.; Fujimori, A.; Barman, S.; Maiti, K.; Sarma, D.; Tokura, Y.; Onoda, M. Electronic Structure of Early 3d-Transition-Metal Oxides by Analysis of the 2p Core-Level Photoemission Spectra. *Phys. Rev. B* **1996**, 53 (3), 1161–1170. <https://doi.org/10.1038/sj.bjp.0704691>.
  - (34) Moradi, Z.; Heydarinasab, A.; Shariati, F. First-principle Study of Doping Effects (Ti, Cu, and Zn) on Electrochemical Performance of Li<sub>2</sub>MnO<sub>3</sub> Cathode Materials for Lithium-ion Batteries. *Int. J. Quantum Chem.* **2021**, 121 (4), e26458.
  - (35) Blöchl, P. E. Projector Augmented-Wave Method. *Phys. Rev. B* **1994**, 50 (24), 17953–17979. <https://doi.org/10.1103/PhysRevB.50.17953>.
  - (36) Nosé, S. A Unified Formulation of the Constant Temperature Molecular Dynamics Methods. *J. Chem. Phys.* **1984**, 81 (1), 511–519. <https://doi.org/10.1063/1.447334>.
  - (37) Hoover, W. Canonical Dynamics: Equilibrium Phase-Space Distributions. *Phys. Rev. A*

- 1985**, 31 (3), 1695–1697. <https://doi.org/10.1103/PhysRevA.31.1695>.
- (38) Akita, T.; Tabuchi, M.; Nabeshima, Y.; Tatsumi, K.; Kohyama, M. Electron Microscopy Analysis of Ti-Substituted Li<sub>2</sub>MnO<sub>3</sub> Positive Electrode before and after Carbothermal Reduction. *J. Power Sources* **2014**, 254, 39–47.
- (39) Tabuchi, M.; Nabeshima, Y.; Takeuchi, T.; Kageyama, H.; Imaizumi, J.; Shibuya, H.; Akimoto, J. Synthesis of High-Capacity Ti-and/or Fe-Substituted Li<sub>2</sub>MnO<sub>3</sub> Positive Electrode Materials with High Initial Cycle Efficiency by Application of the Carbothermal Reduction Method. *J. Power Sources* **2013**, 221, 427–434. <https://doi.org/10.1016/j.jpowsour.2012.08.055>.
- (40) Shannon, R. D.; Prewitt, C. T. Effective Ionic Radii in Oxides and Fluorides. *Acta Crystallogr. Sect. B Struct. Crystallogr. Cryst. Chem.* **1969**, 25 (5), 925–946. <https://doi.org/10.1107/s0567740869003220>.
- (41) Ekoi, E. J.; Gowen, A.; Dorrepaal, R.; Dowling, D. P. Characterisation of Titanium Oxide Layers Using Raman Spectroscopy and Optical Profilometry: Influence of Oxide Properties. *Results Phys.* **2019**, 12 (January), 1574–1585. <https://doi.org/10.1016/j.rinp.2019.01.054>.
- (42) Balachandran, U.; Eror, N. G. Raman Spectra of Titanium Dioxide. *J. Solid State Chem.* **1982**, 42, 276–282.
- (43) Lakshmi-Narayana; Hussain; Mauger; Julien. Transport Properties of Nanostructured Li<sub>2</sub>TiO<sub>3</sub> Anode Material Synthesized by Hydrothermal Method. *Sci* **2019**, 1 (3), 56. <https://doi.org/10.3390/sci1030056>.
- (44) Matsunaga, T.; Komatsu, H.; Shimoda, K.; Minato, T.; Yonemura, M.; Kamiyama, T.; Kobayashi, S.; Kato, T.; Hirayama, T.; Ikuhara, Y.; Arai, H.; Ukyo, Y.; Uchimoto, Y.; Ogumi, Z. Dependence of Structural Defects in Li<sub>2</sub>MnO<sub>3</sub> on Synthesis Temperature. *Chem. Mater.* **2016**, 28 (12), 4143–4150. <https://doi.org/10.1021/acs.chemmater.5b05041>.
- (45) Jarvis, K. A.; Wang, C. C.; Knight, J. C.; Rabenberg, L.; Manthiram, A.; Ferreira, P. J. Formation and Effect of Orientation Domains in Layered Oxide Cathodes of Lithium-Ion Batteries. *Acta Mater.* **2016**, 108, 264–270. <https://doi.org/10.1016/j.actamat.2016.02.034>.
- (46) Shukla, A. K.; Ramasse, Q. M.; Ophus, C.; Duncan, H.; Hage, F.; Chen, G. Unravelling Structural Ambiguities in Lithium- and Manganese-Rich Transition Metal Oxides. *Nat. Commun.* **2015**, 6, 1–9. <https://doi.org/10.1038/ncomms9711>.
- (47) Serrano-sevillano, J.; Carlier, D.; Saracibar, A.; Miguel Lopez del Amo, J.; Casas-Cabanas, M. DFT-Assisted Solid-State NMR Characterization of Defects in Li<sub>2</sub>MnO<sub>3</sub>. *Inorg. Chem.* **2019**, 58, 8347–8356. <https://doi.org/10.1021/acs.inorgchem.9b00394>.
- (48) Grey, C. P.; Lee, Y. J. Lithium MAS NMR Studies of Cathode Materials for Lithium-Ion Batteries. *Solid State Sci.* **2003**, 5 (6), 883–894. [https://doi.org/10.1016/S1293-2558\(03\)00113-4](https://doi.org/10.1016/S1293-2558(03)00113-4).
- (49) Grey, C. P.; Dupre, N. NMR Studies of Cathode Materials for Lithium-Ion Rechargeable Batteries. *Chem. Rev.* **2004**, 104, 4493–4512. <https://doi.org/10.1002/chin.200450214>.
- (50) Marichal, C.; Hirschinger, J.; Granger, P.; Ménétrier, M.; Rougier, A.; Delmas, C. 6Li and 7Li NMR in the LiNi<sub>1-y</sub>Co<sub>y</sub>O<sub>2</sub> Solid Solution (0 ≤ y ≤ 1). *Inorg. Chem.* **1995**, 34 (7), 1773–1778. <https://doi.org/10.1021/ic00111a026>.
- (51) Carewska, M.; Scaccia, S.; Croce, F.; Arumugam, S.; Wang, Y.; Greenbaum, S. Electrical Conductivity and 6,7Li NMR Studies of Li<sub>1+y</sub>CoO<sub>2</sub>. *Solid State Ionics* **1997**, 93, 227–237. [https://doi.org/10.1016/s0167-2738\(96\)00545-0](https://doi.org/10.1016/s0167-2738(96)00545-0).
- (52) Stoyanova, R.; Ivanova, S.; Zhecheva, E.; Samoson, A.; Simova, S.; Tzvetkova, P.; Barra, A. L. Correlations between Lithium Local Structure and Electrochemistry of

- Layered  $\text{LiCo}_{1-2x}\text{Ni}_x\text{Mn}_x\text{O}_2$  Oxides:  $^7\text{Li}$  MAS NMR and EPR Studies. *Phys. Chem. Chem. Phys.* **2014**, *16* (6), 2499–2507. <https://doi.org/10.1039/c3cp54438a>.
- (53) Cho, E.; Kim, K.; Jung, C.; Seo, S. W.; Min, K.; Lee, H. S.; Park, G. S.; Shin, J. Overview of the Oxygen Behavior in the Degradation of  $\text{Li}_2\text{MnO}_3$  Cathode Material. *J. Phys. Chem. C* **2017**, *121* (39), 21118–21127. <https://doi.org/10.1021/acs.jpcc.7b04937>.
- (54) Luo, K.; Roberts, M. R.; Hao, R.; Guerrini, N.; Pickup, D. M.; Liu, Y.; Edström, K.; Guo, J.; Chadwick, A. V.; Duda, L. C.; Bruce, P. G. Charge-Compensation in 3d-Transition-Metal- Oxide Intercalation Cathodes through the Generation of Localized Electron Holes on Oxygen. *Nat. Chem.* **2016**, *8*, 684–691. <https://doi.org/10.1038/nchem.2471>.
- (55) Azcarate, I.; Yin, W.; Méthivier, C.; Ribot, F.; Laberty-Robert, C.; Grimaud, A. Assessing the Oxidation Behavior of EC:DMC Based Electrolyte on Non-Catalytically Active Surface. *J. Electrochem. Soc.* **2020**, *167* (8), 080530. <https://doi.org/10.1149/1945-7111/ab8f57>.
- (56) Urban, A.; Seo, D. H.; Ceder, G. Computational Understanding of Li-Ion Batteries. *npj Comput. Mater.* **2016**, *2*, 16002. <https://doi.org/10.1038/npjcompumats.2016.2>.
- (57) Okubo, M.; Yamada, A. Molecular Orbital Principles of Oxygen-Redox Battery Electrodes. *ACS Appl. Mater. Interfaces* **2017**, *9* (42), 36463–36472. <https://doi.org/10.1021/acsami.7b09835>.
- (58) Shen, S.; Hong, Y.; Zhu, F.; Cao, Z.; Li, Y.; Ke, F.; Fan, J.; Zhou, L.; Wu, L.; Dai, P.; Cai, M.; Huang, L.; Zhou, Z.; Li, J.; Wu, Q.; Sun, S. Tuning Electrochemical Properties of Li-Rich Layered Oxide Cathodes by Adjusting Co/Ni Ratios and Mechanism Investigation Using in Situ X-Ray Diffraction and Online Continuous Flow Differential Electrochemical Mass Spectrometry. *ACS Appl. Mater. Interfaces* **2018**, *10* (15), 12666–12677. <https://doi.org/10.1021/acsami.8b00919>.
- (59) Qi, Z.; Tang, J.; Misra, S.; Fan, C.; Lu, P.; Jian, J.; He, Z.; Pol, V. G.; Zhang, X.; Wang, H. Enhancing Electrochemical Performance of Thin Film Lithium Ion Battery via Introducing Tilted Metal Nanopillars as Effective Current Collectors. *Nano Energy* **2020**, *69* (October 2019). <https://doi.org/10.1016/j.nanoen.2019.104381>.
- (60) Croy, J. R.; Kim, D.; Balasubramanian, M.; Gallagher, K.; Kang, S.-H.; Thackeray, M. M. Countering the Voltage Decay in High Capacity  $\text{XLi}_2\text{MnO}_3 \cdot (1-x)\text{LiMO}_2$  Electrodes (M=Mn, Ni, Co) for Li<sup>+</sup>-Ion Batteries. *J. Electrochem. Soc.* **2012**, *159* (6), A781–A790. <https://doi.org/10.1149/2.080206jes>.
- (61) Pires, J.; Timperman, L.; Castets, A.; Peña, J. S.; Dumont, E.; Levasseur, S.; Dedryvère, R.; Tessier, C.; Anouti, M. Role of Propane Sultone as an Additive to Improve the Performance of a Lithium-Rich Cathode Material at a High Potential. *RSC Adv.* **2015**, *5* (52), 42088–42094. <https://doi.org/10.1039/c5ra05650k>.
- (62) Zhao, W.; Xiong, L.; Xu, Y.; Li, H.; Ren, Z. High Performance  $\text{Li}_2\text{MnO}_3/\text{RGO}$  Composite Cathode for Lithium Ion Batteries. *J. Power Sources* **2017**, *349*, 11–17. <https://doi.org/10.1016/j.jpowsour.2017.03.022>.
- (63) Assat, G.; Foix, D.; Delacourt, C.; Iadecola, A.; Dedryvère, R.; Tarascon, J. Fundamental Interplay between Anionic/Cationic Redox Governing the Kinetics and Thermodynamics of Lithium-Rich Cathodes. *Nat. Commun.* **2017**, *8*, 1–12. <https://doi.org/10.1038/s41467-017-02291-9>.
- (64) Benedek, R. First-Cycle Simulation for Li-Rich Layered Oxide Cathode Material  $\text{XLi}_2\text{MnO}_3 \cdot (1-x)\text{LiMO}_2$  ( $x=0.4$ ). *J. Electrochem. Soc.* **2018**, *165* (11), A2667–A2674. <https://doi.org/10.1149/2.0671811jes>.
- (65) Benedek, R.; Iddir, H. Simulation of First-Charge Oxygen-Dimerization and Mn-Migration in Li-Rich Layered Oxides  $\text{XLi}_2\text{MnO}_3 \cdot (1-X)\text{LiMO}_2$  and Implications for

- Voltage Fade. *J. Phys. Chem. C* **2017**, *121* (12), 6492–6499.  
<https://doi.org/10.1021/acs.jpcc.7b00277>.
- (66) Gao, Y.; Ma, J.; Wang, Z.; Lu, G.; Chen, L. Vacancy-Induced MnO<sub>6</sub> Distortion and Its Impacts on Structural Transition of Li<sub>2</sub>MnO<sub>3</sub>. *Phys. Chem. Chem. Phys.* **2017**, *19* (10), 7025–7031. <https://doi.org/10.1039/c6cp08441a>.
- (67) Gent, W. E.; Lim, K.; Liang, Y.; Li, Q.; Barnes, T.; Ahn, S. J.; Stone, K. H.; McIntire, M.; Hong, J.; Song, J. H.; Li, Y.; Mehta, A.; Ermon, S.; Tyliszczak, T.; Kilcoyne, D.; Vine, D.; Park, J. H.; Doo, S. K.; Toney, M. F.; Yang, W.; Prendergast, D.; Chueh, W. C. Coupling between Oxygen Redox and Cation Migration Explains Unusual Electrochemistry in Lithium-Rich Layered Oxides. *Nat. Commun.* **2017**, *8* (1), 1–12.  
<https://doi.org/10.1038/s41467-017-02041-x>.
- (68) Chen, H.; Islam, M. S. Lithium Extraction Mechanism in Li-Rich Li<sub>2</sub>MnO<sub>3</sub> Involving Oxygen Hole Formation and Dimerization. *Chem. Mater.* **2016**, *28*, 6656–6663.  
<https://doi.org/10.1021/acs.chemmater.6b02870>.
- (69) Croy, J. R.; Iddir, H.; Gallagher, K.; Johnson, C. S.; Benedek, R.; Balasubramanian, M. First-Charge Instabilities of Layered-Layered Lithium-Ion-Battery Materials. *Phys. Chem. Chem. Phys.* **2015**, *17* (37), 24382–24391. <https://doi.org/10.1039/c5cp02943k>.
- (70) Morozov, A. V.; Moiseev, I. A.; Savina, A. A.; Boev, A. O.; Aksyonov, D. A.; Zhang, L.; Morozova, P. A.; Nikitina, V. A.; Pazhetnov, E. M.; Berg, E. J.; Fedotov, S. S.; Tarascon, J. M.; Antipov, E. V.; Abakumov, A. M. Retardation of Structure Densification by Increasing Covalency in Li-Rich Layered Oxide Positive Electrodes for Li-Ion Batteries. *Chem. Mater.* **2022**, *34* (15), 6779–6791.  
<https://doi.org/10.1021/acs.chemmater.2c00921>.



## Supporting Information

### Understanding the Activation of Anionic Redox Chemistry in $\text{Ti}^{4+}$ - Substituted $\text{Li}_2\text{MnO}_3$ as a Cathode Material for Li-Ion Batteries

Andreas Paulus<sup>a,b\*</sup>, Mylène Hendrickx<sup>c</sup>, Selma Mayda<sup>c</sup>, Maria Batuk<sup>c</sup>, Gunter Reekmans<sup>d</sup>,  
Miriam von Holst<sup>a</sup>, Ken Elen<sup>a,b</sup>, Artem M. Abakumov<sup>e,c</sup>, Peter Adriaensens<sup>d</sup>, Dirk Lamoen<sup>c</sup>,  
Bart Partoens<sup>f</sup>, Joke Hadermann<sup>c</sup>, Marlies K. Van Bael<sup>a,b</sup> and An Hardy<sup>a,b\*</sup>

<sup>a</sup>Hasselt University, Institute for Materials Research (imo-imomec) and imec, division imomec, Materials Chemistry, DESINE group, Agoralaan Gebouw D, 3590 Diepenbeek, Belgium

<sup>b</sup>EnergyVille, Thor Park 8320, 3600 Genk, Belgium

<sup>c</sup>University of Antwerp, Electron Microscopy for Materials Science (EMAT), Groenenborgerlaan 171, 2020 Antwerpen, Belgium

<sup>d</sup>Hasselt University, Institute for Materials Research (imo-imomec), NMR group, Agoralaan Gebouw D, 3590 Diepenbeek, Belgium

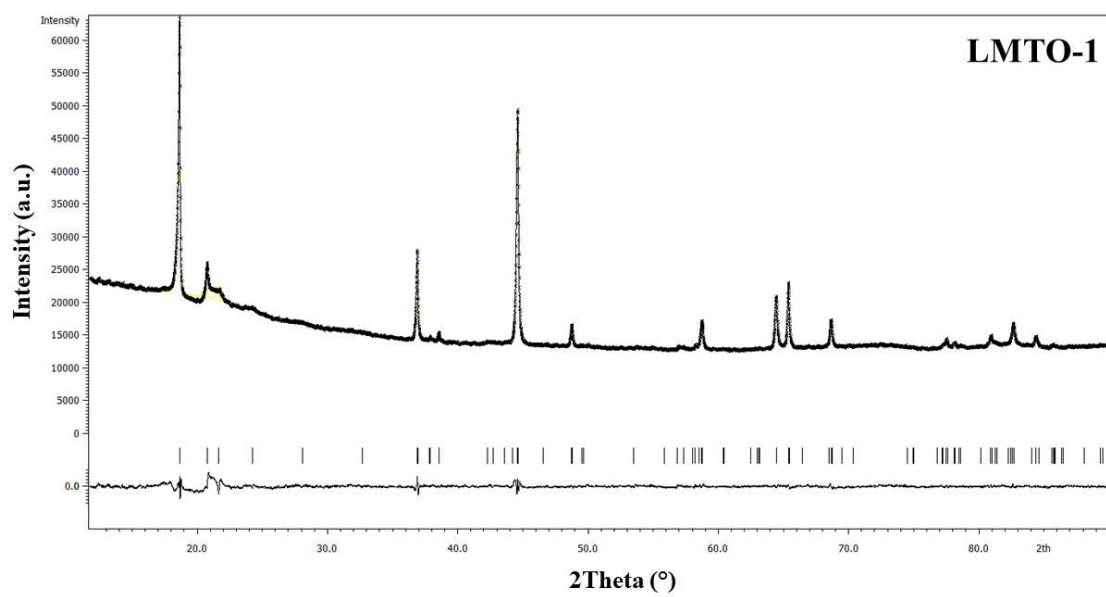
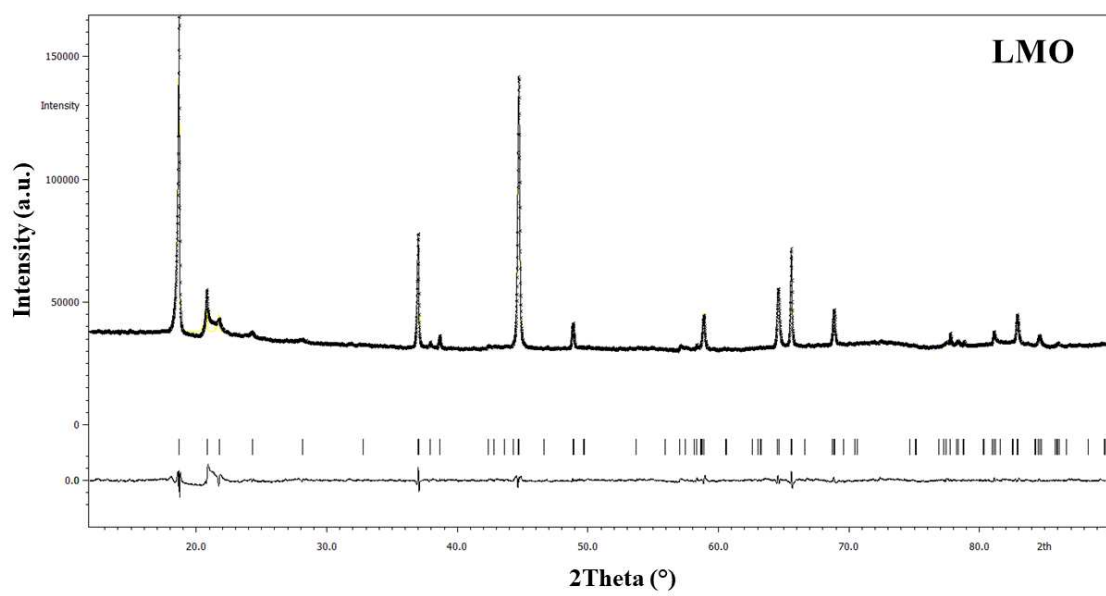
<sup>e</sup>Center for Energy Science and Technology, Skolkovo Institute of Science and Technology, 3 Nobel Street, Moscow 143026, Russia

<sup>f</sup>University of Antwerp, Condensed Matter Theory (CMT), Groenenborgerlaan 171, 2020 Antwerpen, Belgium

Corresponding authors \*:

[andreas.paulus@uhasselt.be](mailto:andreas.paulus@uhasselt.be)

[an.hardy@uhasselt.be](mailto:an.hardy@uhasselt.be)



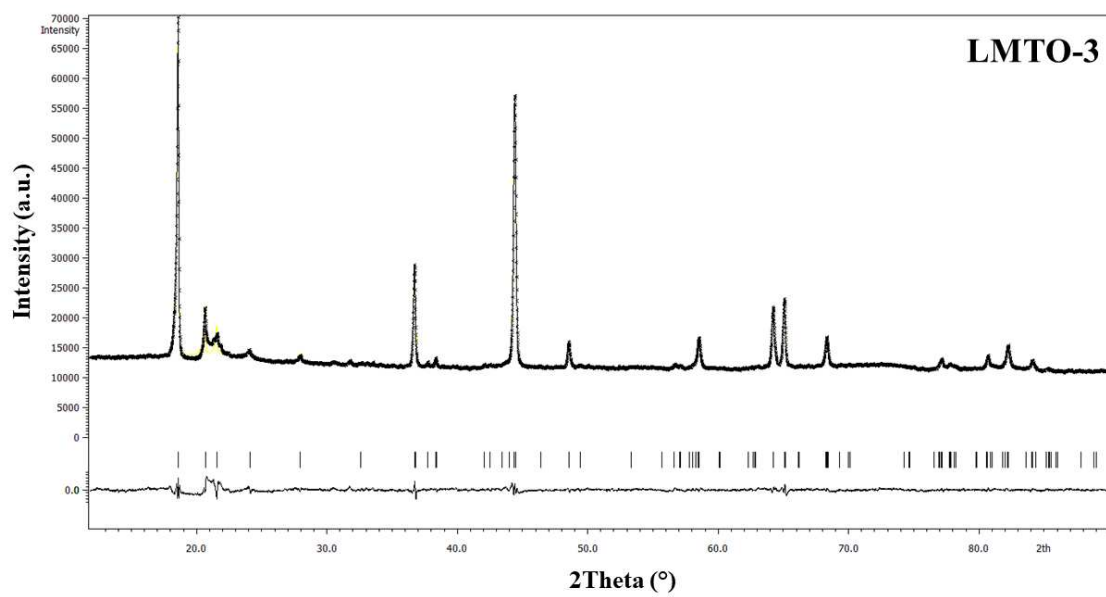
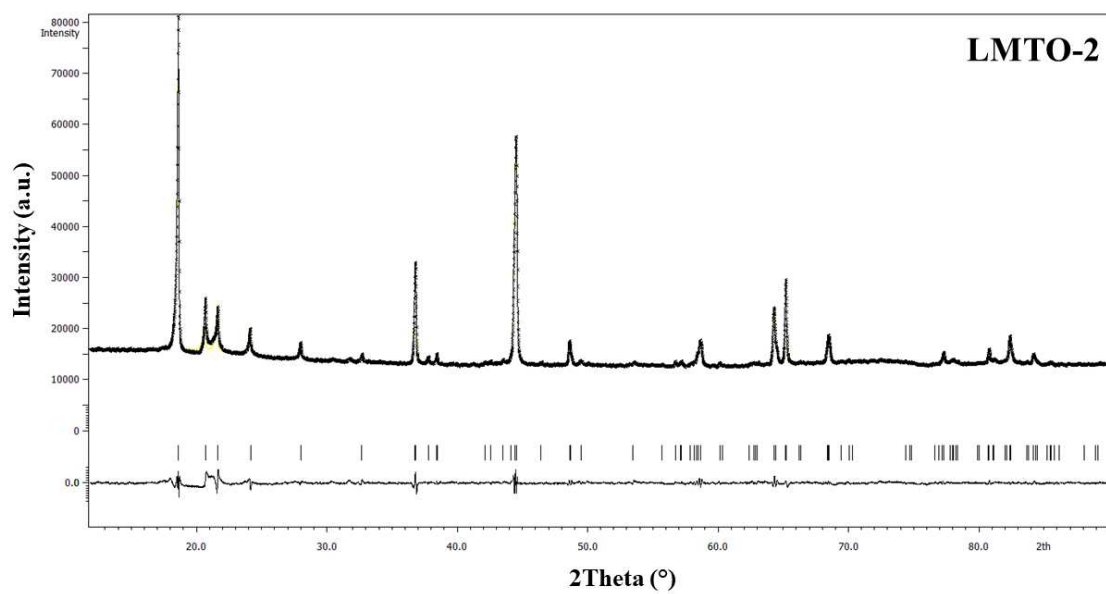


**Figure S1.** PXRD patterns of the LMO, LMT0-1, LMT0-2 and LMT0-3 samples after fitting with the Le Bail method. The reflection positions are marked by the vertical bars, corresponding to the monoclinic  $C2/m$  unit cell.

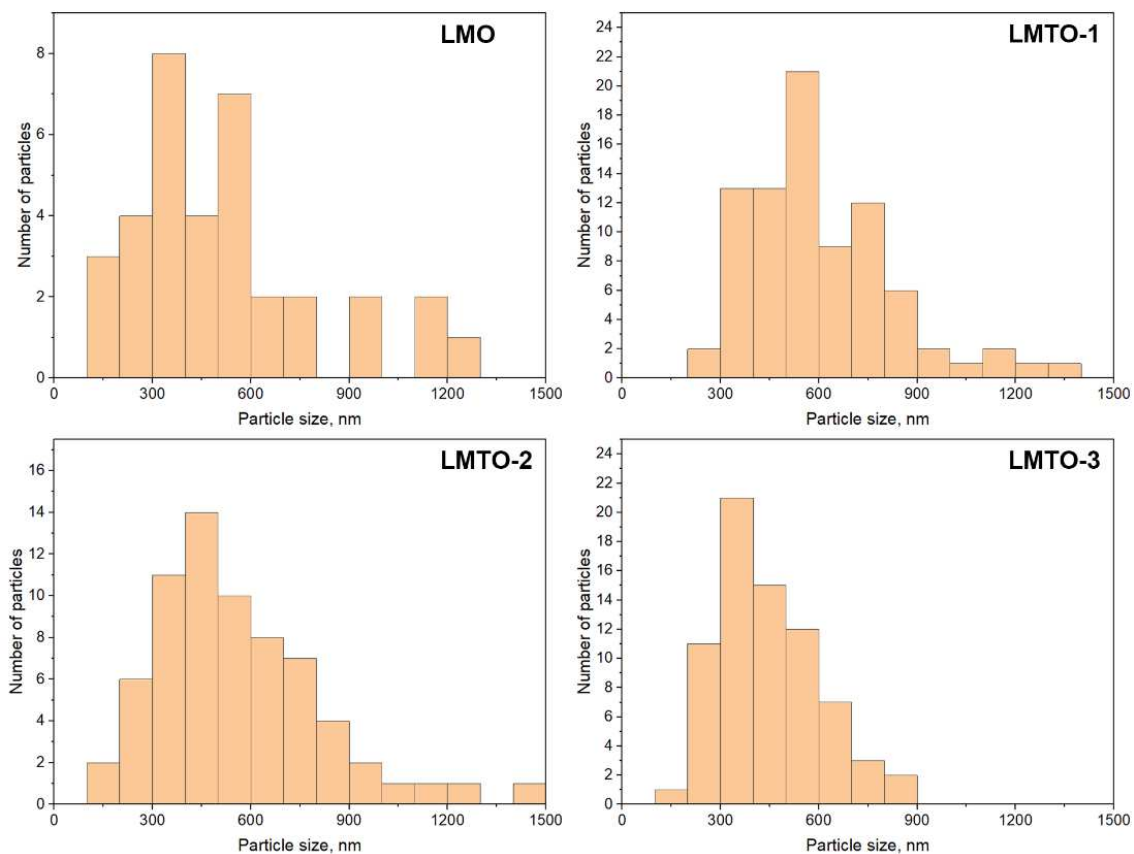


**Figure S2.** Particle size distribution in the LMO, LMTO-1, LMTO-2 and LMTO-3 samples. Particles of both morphologies (smooth and rough) were included in the calculations. For the particles of the irregular shape, the longest dimension was measured.

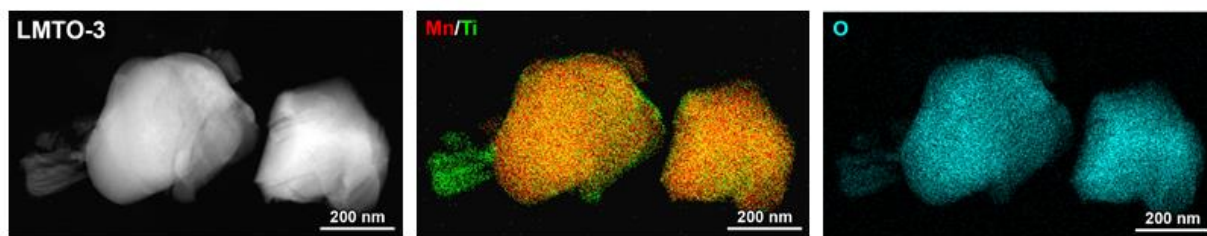


**Figure S3.** HAADF-STEM image and corresponding STEM-EDX mixed {Mn, Ti} and individual O elemental maps of representative particles in the LMTO-3 sample, including a particle for which only Ti and O peaks were detected.

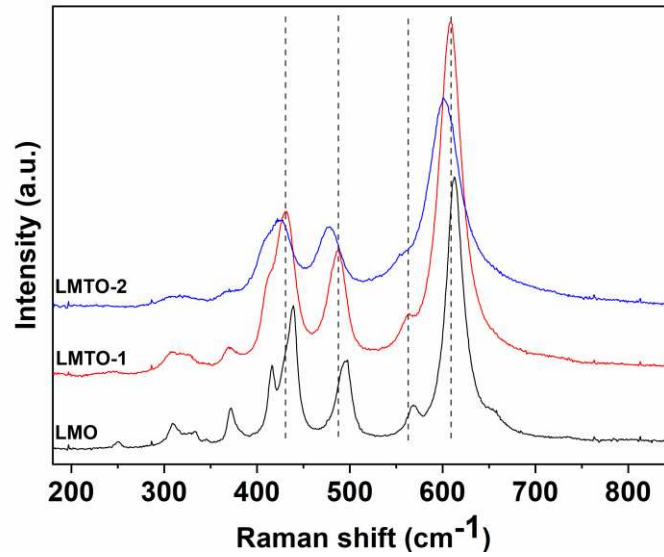


**Figure S4.** Raman spectra of LMO, LMTO-1 and LMTO-2 samples. Dashed lines are a guide to the eye to indicate the red shift upon increasing Ti content.

The Raman spectrum of  $\text{TiO}_2$  (rutile) is characterized by two main peaks at around  $448 \text{ cm}^{-1}$  and  $612 \text{ cm}^{-1}$  (respectively  $E_g$  and  $A_{1g}$  normal modes) and a moderately strong broad band with maximum at  $\sim 235 \text{ cm}^{-1}$ . The Raman spectrum of the end-member  $\text{Li}_2\text{TiO}_3$  ( $x=1$  in  $\text{Li}_2\text{Mn}_{1-x}\text{Ti}_x\text{O}_3$ ) is characterized by four main normal modes at  $358 \text{ cm}^{-1}$ ,  $409 \text{ cm}^{-1}$ ,  $430 \text{ cm}^{-1}$  and  $668 \text{ cm}^{-1}$  respectively. Both likely impurity phases were not detected.

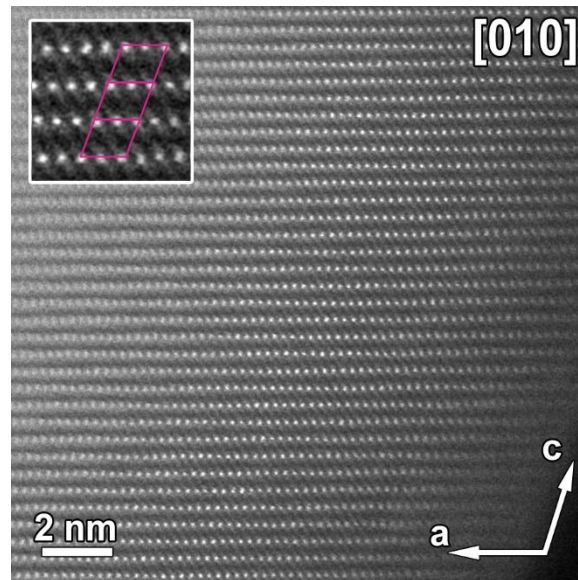


**Figure S5.** HAADF-STEM image along the  $[010]$  orientation obtained from the LMTO-1 sample. The bright atomic columns correspond to Mn/Ti atoms, whereas Li and O columns are too light to be seen in the image. The inset indicates the unit cells corresponding to the  $C2/m$  symmetry. Some bright dots are observed in the lithium layer, as can be seen in the inset.

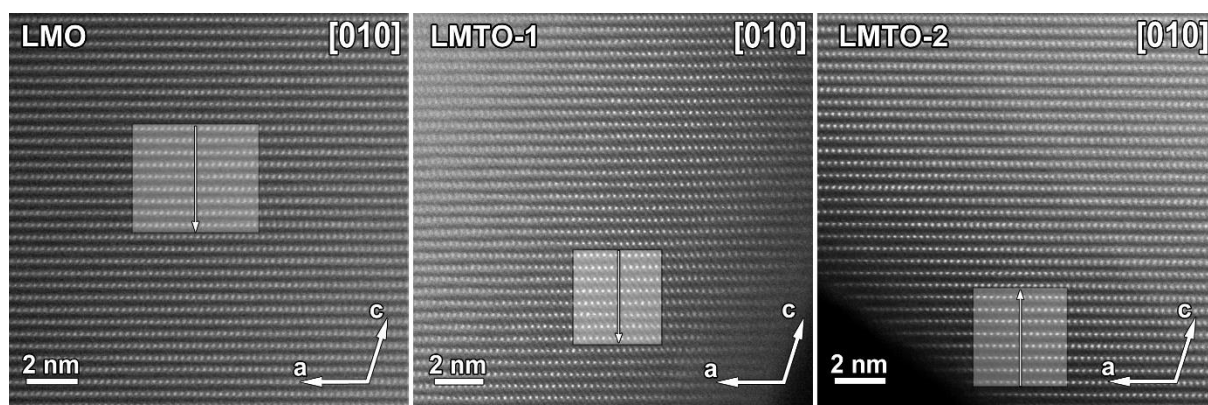


**Figure S6.** HAADF-STEM image along the [010] orientation obtained from the LMO, LMTO-1 and LMTO-2 samples. The grey areas mark the regions of which a line profile has been taken. The corresponding line profiles are shown in **Figure S7**.

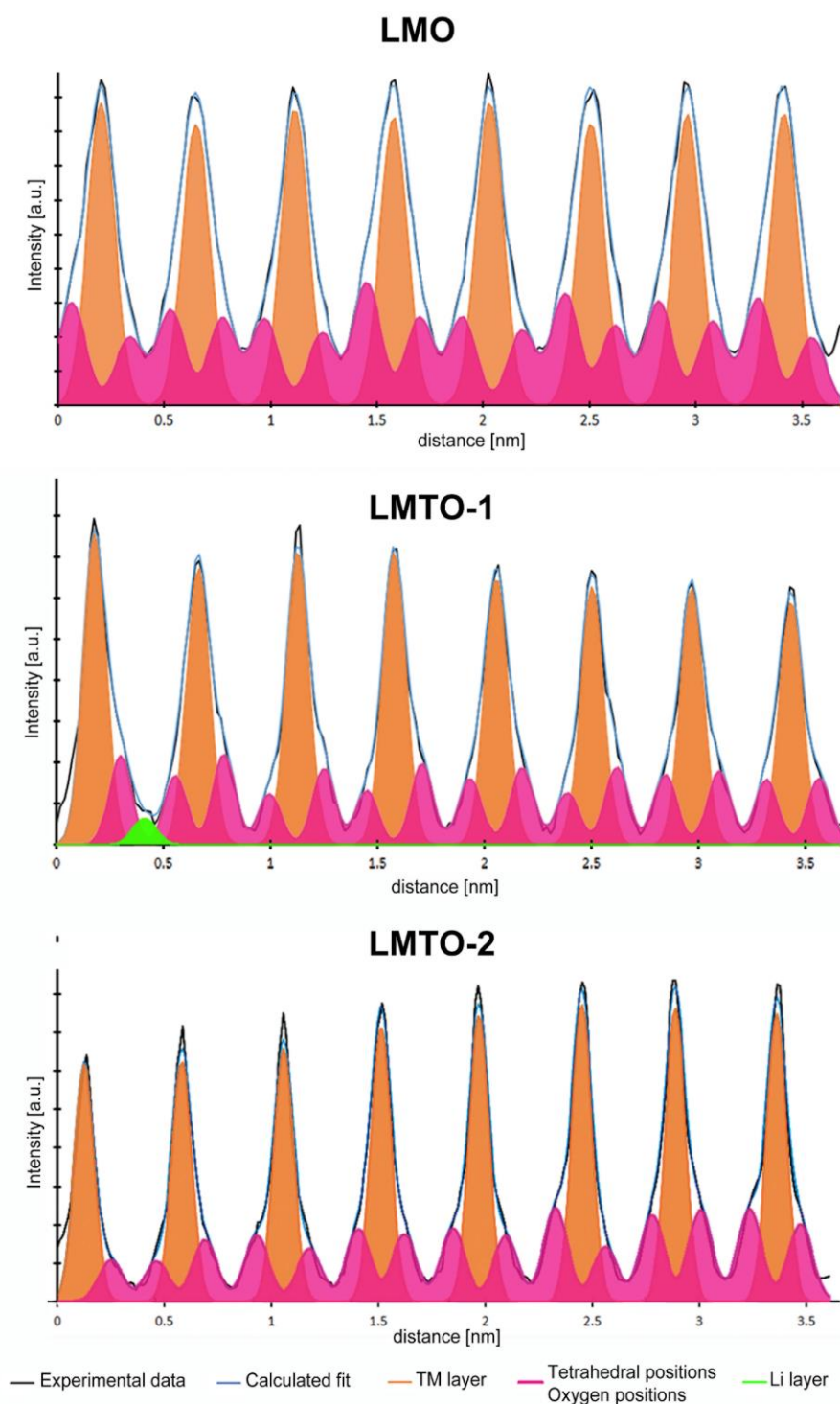


**Figure S7.** Line profiles taken from the areas marked in **Figure S6**, perpendicular to the layers in the HAADF-STEM image along the [010] direction for LMO, LMTO-1 and LMTO-2. Every peak represents an averaged atom column. The intensity of the peaks represented by ‘TM layer’ and ‘Li layer’ is associated to the presence of transition metals, while the intensity of the pink peaks is attributed to both the transition metals in the tetrahedral interstices and the oxygen atoms.

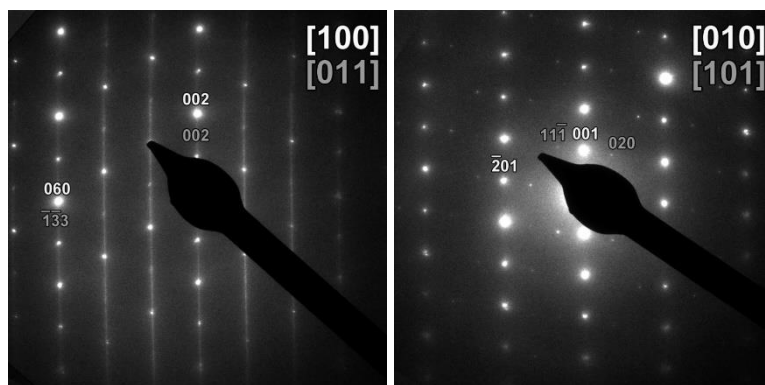


**Figure S8.** SAED patterns taken from the LMTO-1 sample show that the particle consists of domains with different orientations. The left SAED pattern shows domains that correspond to the [100] and [011] orientation; the right SAED pattern shows domains that correspond to the [010] and [101] orientations. For each pattern, the different orientations are equivalent in the parent cubic structure ( $Fm-3m$ ) where the TM and Li are randomly distributed.

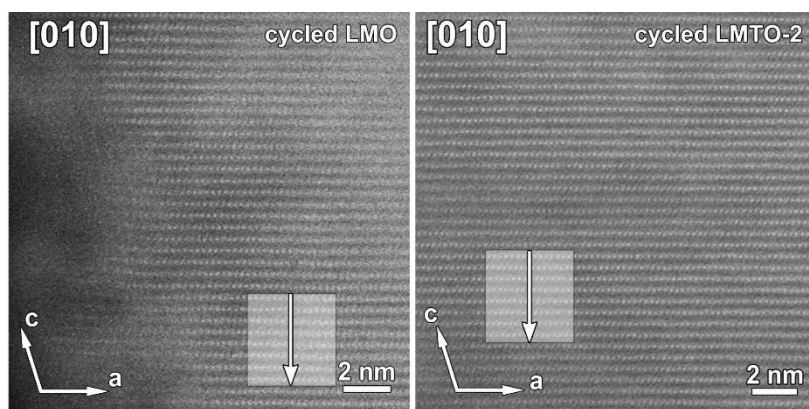


**Figure S9.** HAADF-STEM image along the [010] orientation obtained from the cycled LMO and LMTO-2 samples. The grey areas mark the regions of which a line profile has been taken. The corresponding line profiles are shown in **Figure S10**.



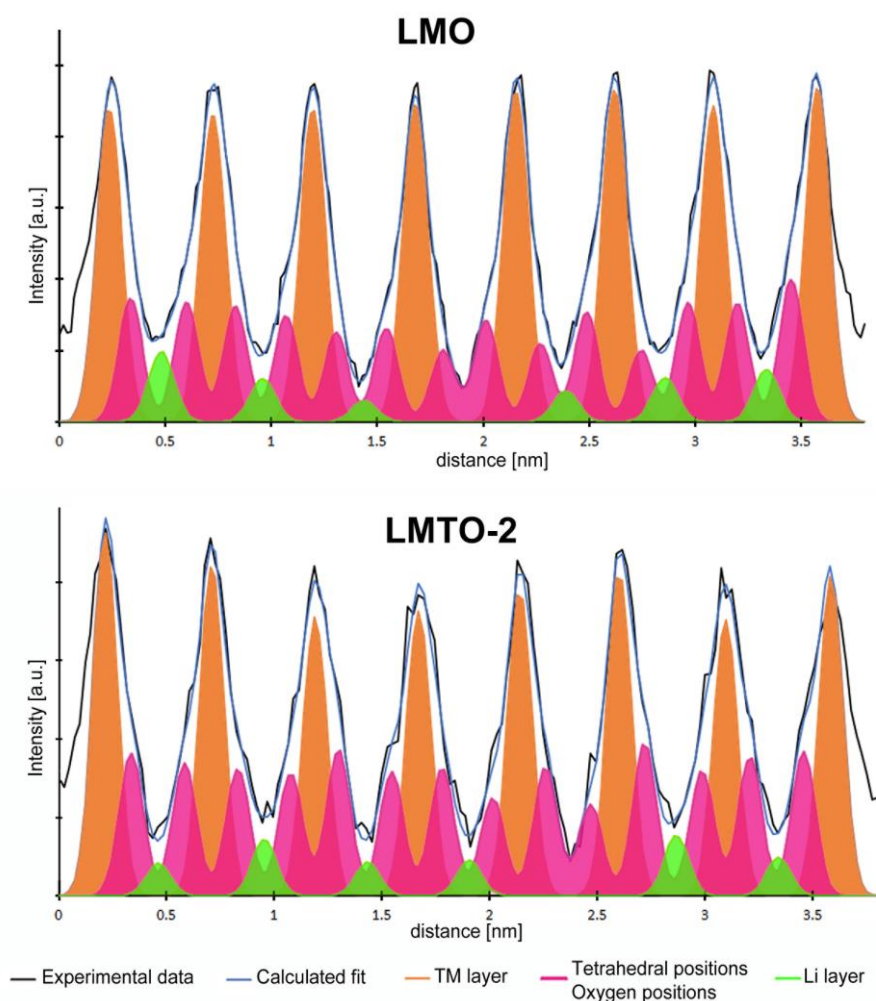


**Figure S10.** Line profiles taken from the areas marked in **Figures S9**, perpendicular to the layers in the HAADF-STEM image along the [010] direction for respectively cycled LMO and LMTO-2. Every peak represents an averaged atom column. The intensity of the peaks represented by ‘TM layer’ and ‘Li layer’ is associated to the presence of transition metals, while the intensity of the pink peaks is attributed to both the transition metals in the tetrahedral interstices and the oxygen atoms.

### QSTEM simulation for line profiles

In order to analyze the amount of TM migration at both the Li positions and the tetrahedral positions, line profiles were taken perpendicular to the layers in the HAADF-STEM images along the [010] orientation from the LMO, LMTO-1 and LMTO-2 samples, marked in **Figure S6** and **Figure S9**. The line profiles are shown in **Figure S7** and **Figure S10**. The peaks in the experimental data are fitted by Gaussian functions using the program Fityk [1]. All the peaks corresponding to the mixed TM-Li layers (peaks represented by "TM layer") are refined with the same full width half maximum (FWHM). Since the lithium atoms ( $Z = 3$ ) are not visible in the HAADF-STEM images, the peaks observed in the lithium layers (peaks represented by "Li layer") entirely originate from the presence of transition metals. Therefore, these peaks are refined with the same FWHM as the peaks in the TM layer. The intensity of these peaks provides information about the amount of TM migration towards the lithium layer. The peaks corresponding to the position between these two layers correspond to either the oxygen positions or the empty tetrahedral holes, which means that these peaks can give information

about the number of transition metals trapped in the tetrahedral holes. Oxygen atoms ( $Z = 8$ ) are expected to be too light to visualize in the HAADF-STEM images due to the contrast  $I \sim Z^2$ , however, if the other elements also have low atomic numbers, such as Mn ( $Z = 25$ ), the oxygen atoms contribute to the intensity of these peaks. This is clear from the line profiles taken from the pristine LMO, LMTO-1 and LMTO-2 samples, where clear peaks were observed at these positions, while in the pristine structure no transition metals are expected at the tetrahedral positions. In order to verify the actual contribution of these peaks, HAADF-STEM simulations have been made to compare the line profiles to the experimental data.

HAADF-STEM images along the [010] orientation were simulated with the program QSTEM [2] with two different thicknesses: 27 Å and 98.5 Å shown in **Figure S11**. The line profiles reveal the significant contribution of the oxygen atom columns to these peaks, where the intensity increases concomitantly with increasing thickness. On the other hand, the intensity of these peaks will also be affected by the number of transition metals trapped in the tetrahedral holes. Therefore, HAADF-STEM images were simulated with 0% and 10% of the total amount of transition metals that are migrated towards the tetrahedral holes, using a constant thickness of 98.5 Å (**Figure S11**). The peak intensity significantly increases together with increasing the occupancy of the tetrahedral holes. Unfortunately, combining both the variation in thickness and the occupancy makes it impossible to derive the correct amount of TM migration towards the tetrahedral holes, and one can only suggest their presence based on variations in brightness among the peaks themselves.

In addition, HAADF-STEM images were simulated with 0% and 10% of the total amount of transition metals that are migrated towards the lithium layers, using a constant thickness of 98.5 Å (**Figure S11**). The simulations show that TM migration lower than 5% will be difficult to detect; especially when the thickness increases and the intensity of the neighboring peaks increases due to the contribution of the oxygen atom columns.

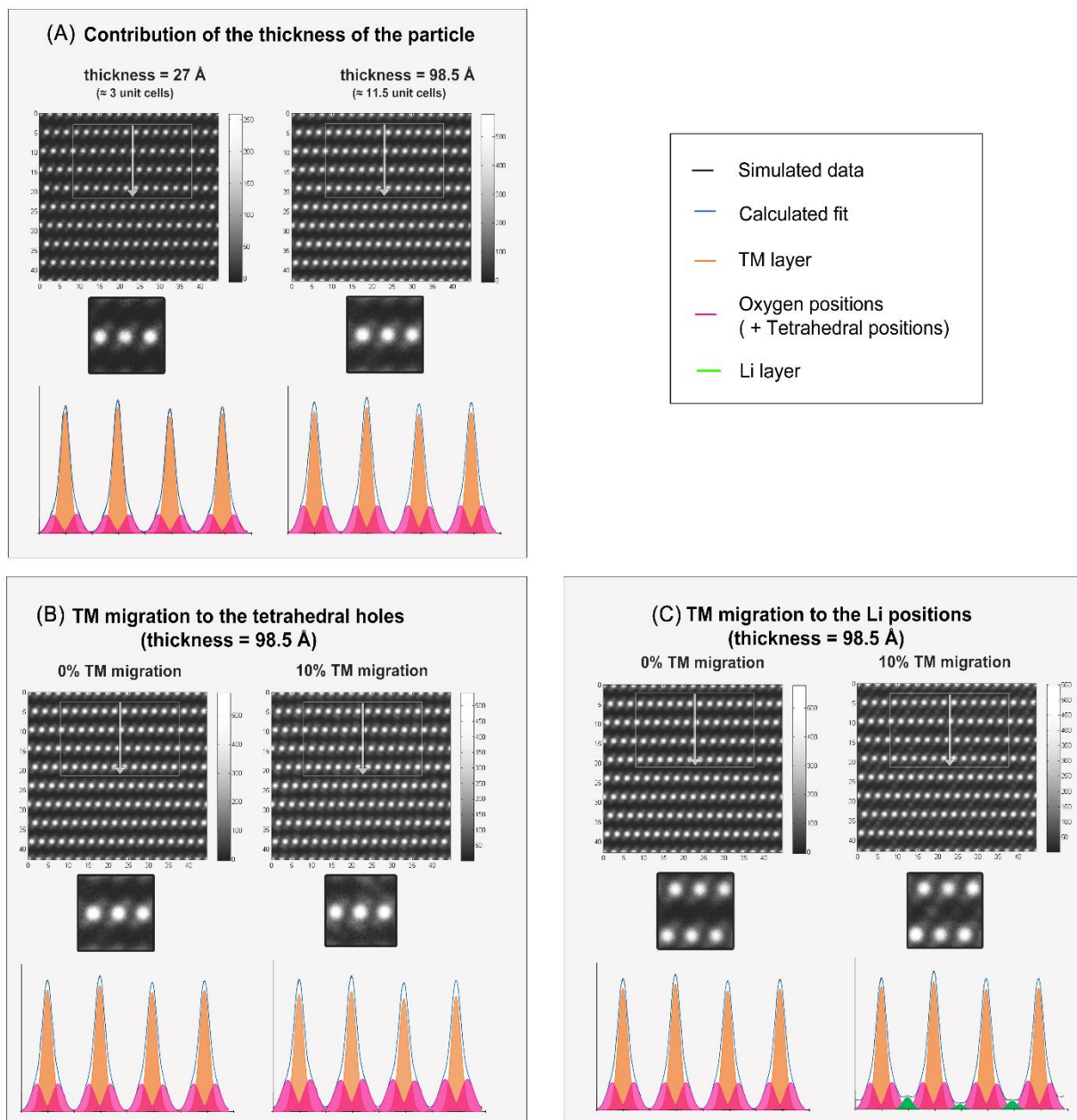


**Figure S11.** Simulation of the HAADF-STEM image along the [010] orientation of the pristine structure for a thickness of 98.5 Å, where the TM migration varies with respectively 0% and 10%. In the model, TM atoms are added to the tetrahedral positions (left) or Li positions (right), while the same amount of TM is removed from the honeycomb layer. The HAADF-STEM images are simulated using QSTEM [2].

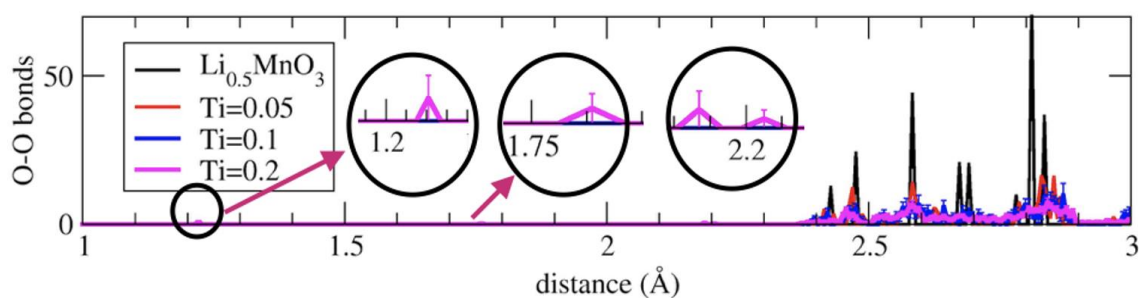


**Figure S12.** O-O distance for  $\text{Li}_{0.5}\text{Mn}_{1-x}\text{Ti}_x\text{O}_3$ . The ellipses amplify the O-O dimer formation and O-O bonds at 2.2 Å for  $x=0.2$  concentration.

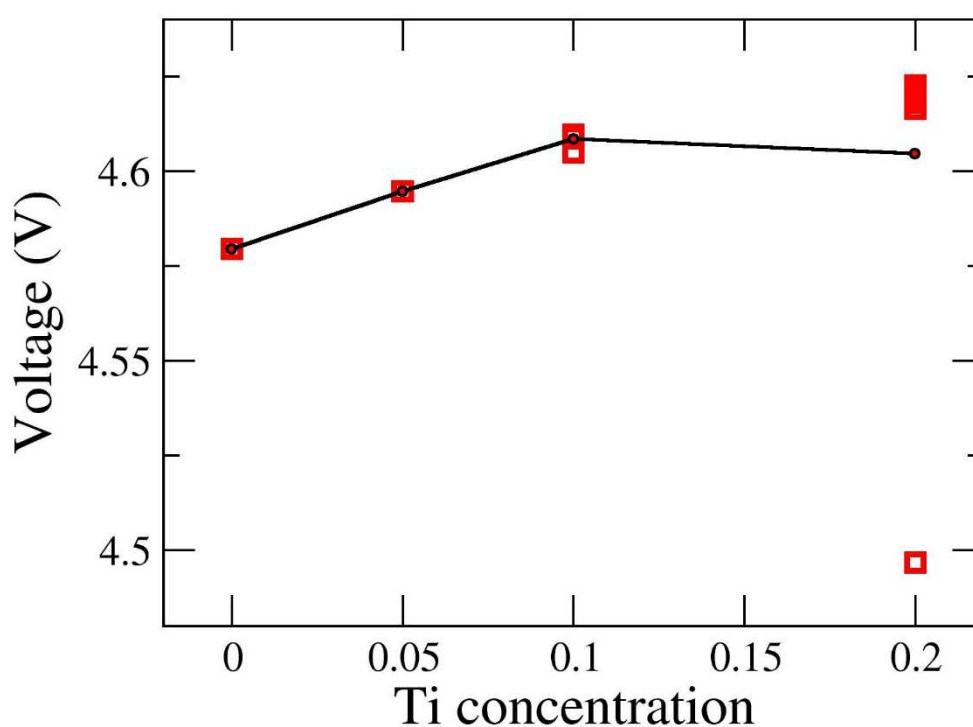


**Figure S13.** Lithium extraction voltage (V) for LMO, LMTO-05, LMTO-1 and LMTO-2. Here, 0 concentration is LMO, 0.05 concentration is LMTO-05, 0.1 concentration is LMTO-1 and 0.2 concentration is LMTO-2. The red dots were shown different configurations for  $x=0.1$  and 0.2 concentrations. The black lines are the average of the V. For LMTO-2 (Ti=0.2 concentration), one voltage value for on configuration is very small with respect to others. This is because a simultaneous dimer formation occurs in this structure and this dimer formation decreases V value.

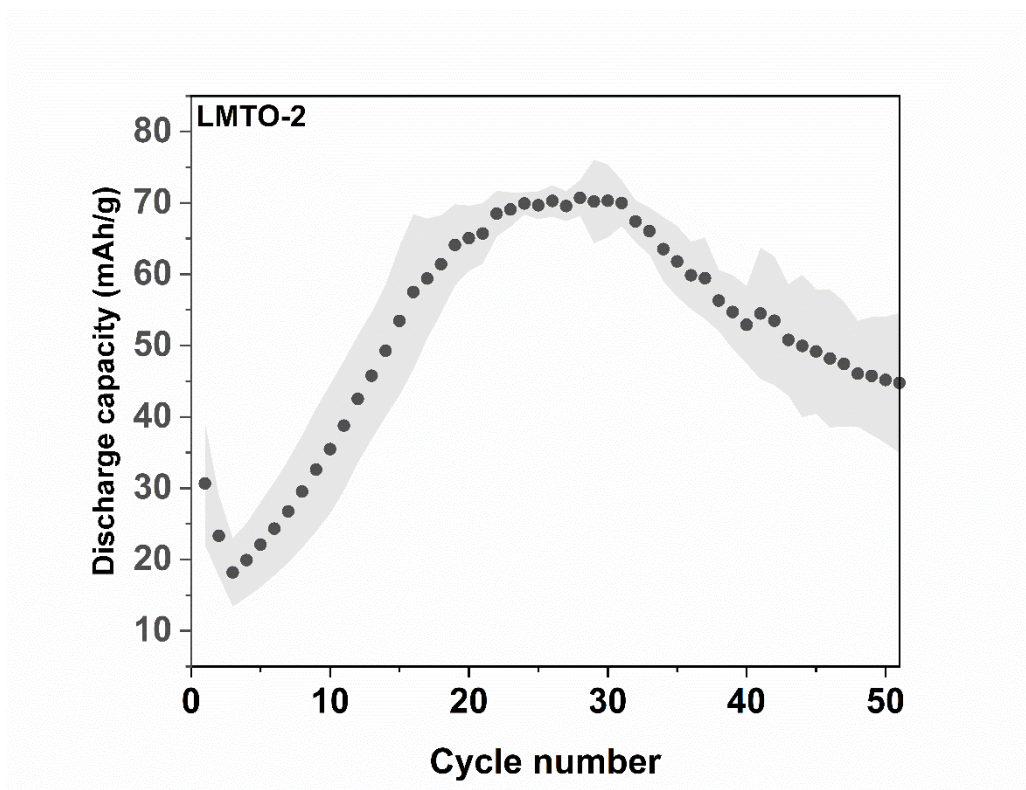


**Figure S14.** Discharge capacity vs. cycle number for LMTO-2, averaged over three coin cells. The standard deviation is represented by filled area surrounding the averaged data points.

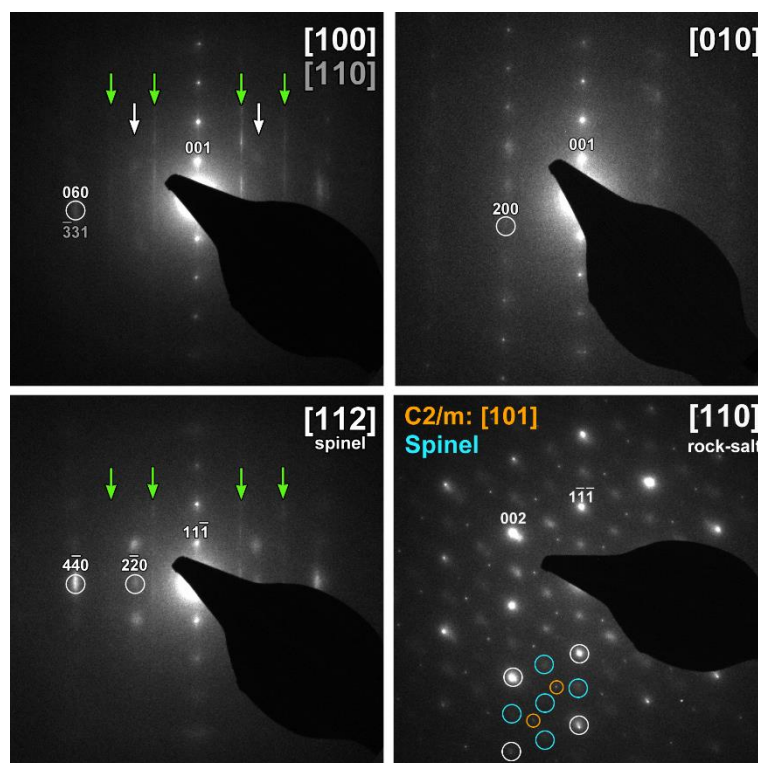


**Figure S15.** SAED patterns of the cycled LMO sample, taken along the [100]/[110] and [010] orientation in the  $C2/m$  symmetry, where the two top patterns show that the  $C2/m$  symmetry is mainly

preserved, in which the white arrows indicate the diffuse reflections that arise from the formation of the spinel structure, while the two bottom patterns show the same [100]/[110] and [010] orientations but already degraded to the spinel and rock-salt structure, respectively. The top SAED and bottom left SAED patterns are obtained from the same particle, showing that the structure does not degrade homogeneously during electrochemical cycling. The SAED pattern indexed in the [110] orientation of the rock-salt structure also shows some diffuse reflections corresponding to the spinel structure (blue circles), and the sharp reflection marked by orange circles show the presence of a separate domain that still preserves the  $C2/m$  symmetry. For the latter SAED pattern, calculated ED patterns corresponding to the different domains and symmetries are shown in **Figure S16**.

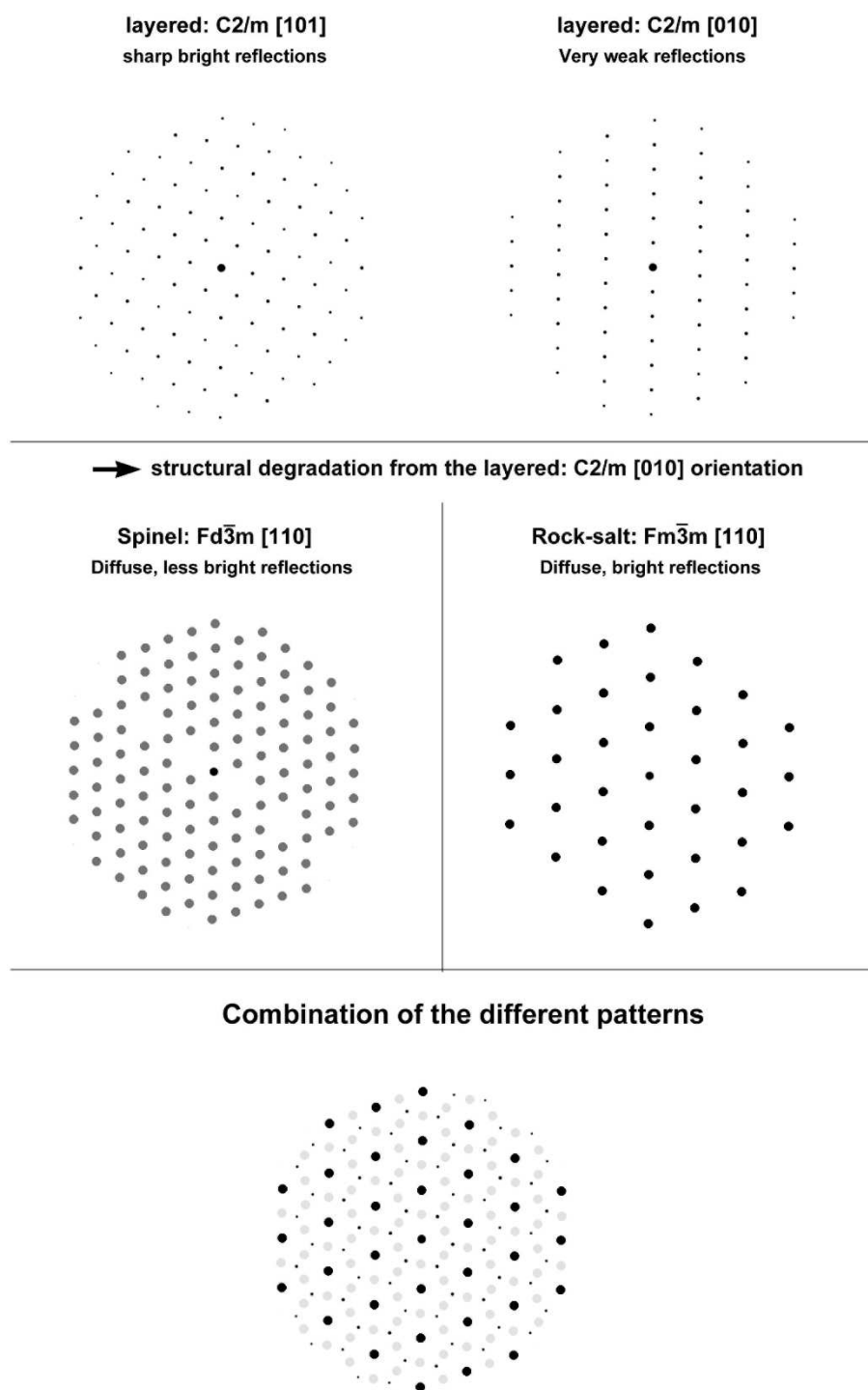




**Figure S16.** The different calculated ED patterns that are present in the experimental SAED patterns at the bottom right in **Figure S15** are shown separately and combined as in the experimental SAED pattern. Top: the SAED patterns along the two orientation  $[101]$  and  $[010]$  in the  $C2/m$  structure. Middle: SAED patterns along the  $[110]$  orientation in the spinel structure  $Fd-3m$  and the rock-salt structure  $Fm-3m$  (equivalent to  $[010]$  in the  $C2/m$  structure). The domains corresponding to  $[010]$  in the  $C2/m$  structure are degraded to these SAED patterns in the spinel and rock-salt structure. Bottom: The combined SAED patterns comparable to the experimental pattern in **Figure S15**.

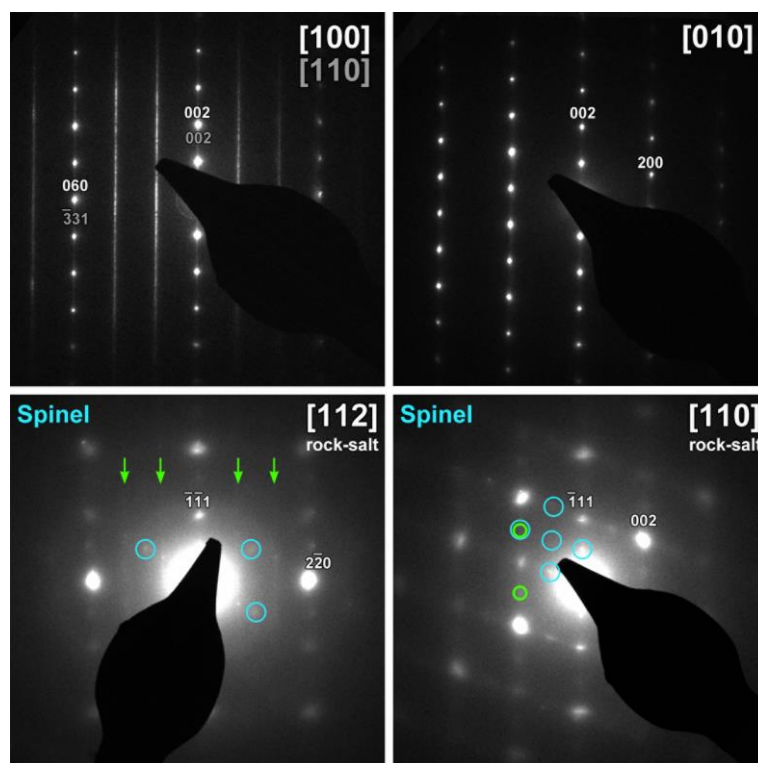


**Figure S17.** SAED patterns of the cycled LMTO-2 sample, taken from two different particles divided in top and bottom. The top SAED patterns taken along the  $[010]$  and  $[100]/[110]$  orientations could be indexed in the monoclinic  $C2/m$  symmetry, indicating the layered structure is preserved for this particular particle. The bottom two SAED patterns could be indexed in the rock-salt structure. The indexed reflections are present in the three different structures: layered, spinel and rock-salt, but for both the layered and spinel structure, additional reflections should be present. The weak streaks and reflections that correspond to the  $C2/m$  symmetry are marked by green arrows and circles respectively, while the blue circles show the weak reflections that could only be indexed by the spinel structure. The indexed reflections are much brighter than those marked by arrows or circles, which indicates that the particle has partially changed to a rock-salt structure where the structure has mixed Li and TM positions. Nevertheless, the weak reflections marked by the arrows (resp. circles), reveal that a small part of the particle still has a layered (resp. spinel) structure.

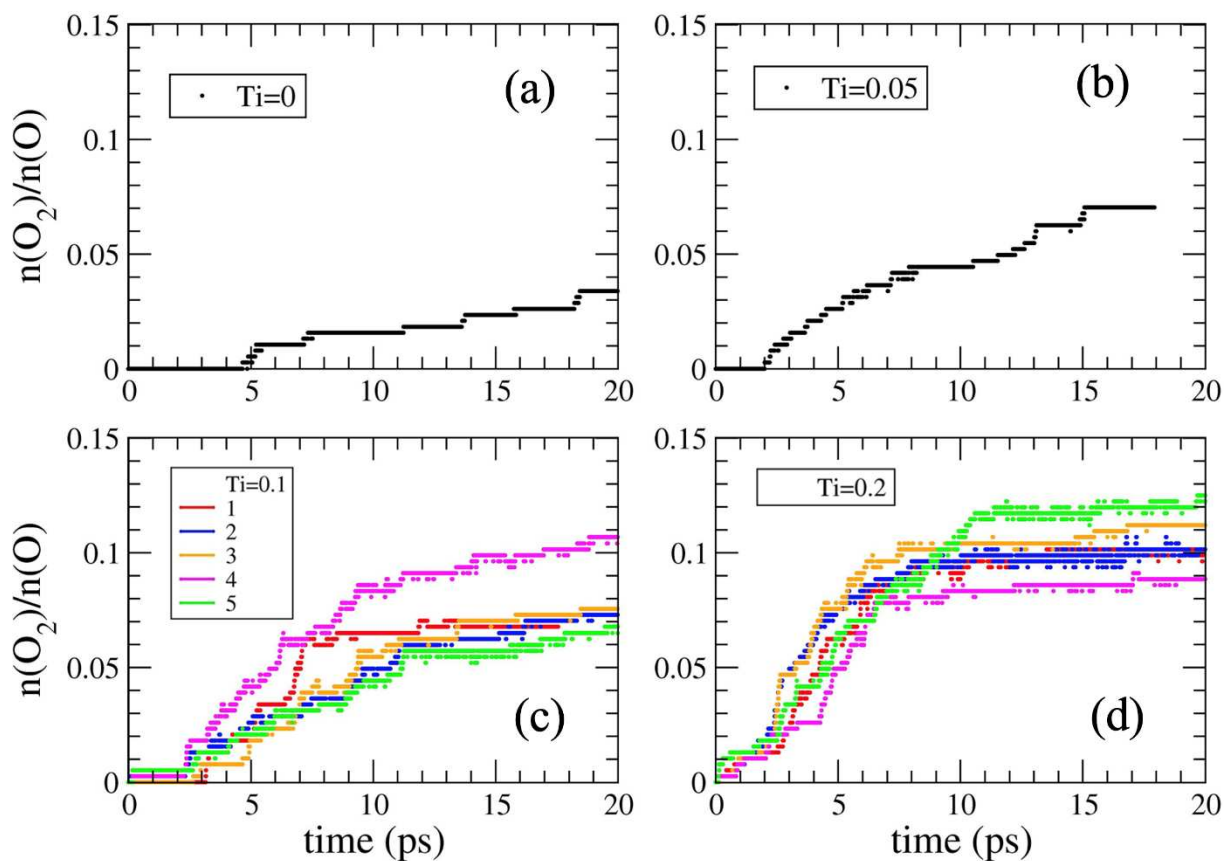


**Figure S18.** O-O dimer fraction with respect to the MD time step for (a) LMO, (b) LMTO-05, (c) LMTO-1 and (d) LMTO-2 at 300 K. For LMTO-1 and LMTO-2 structures, 5 different MD simulations were performed. The colored lines show the dimer fractions of each structure. Here, time steps are in ps.  $n(\text{O}_2)$  is the total number of dimers and  $n(\text{O})$  is the total number of oxygen atoms in the structures. The dimer fraction is  $n(\text{O}_2)/n(\text{O})$ .



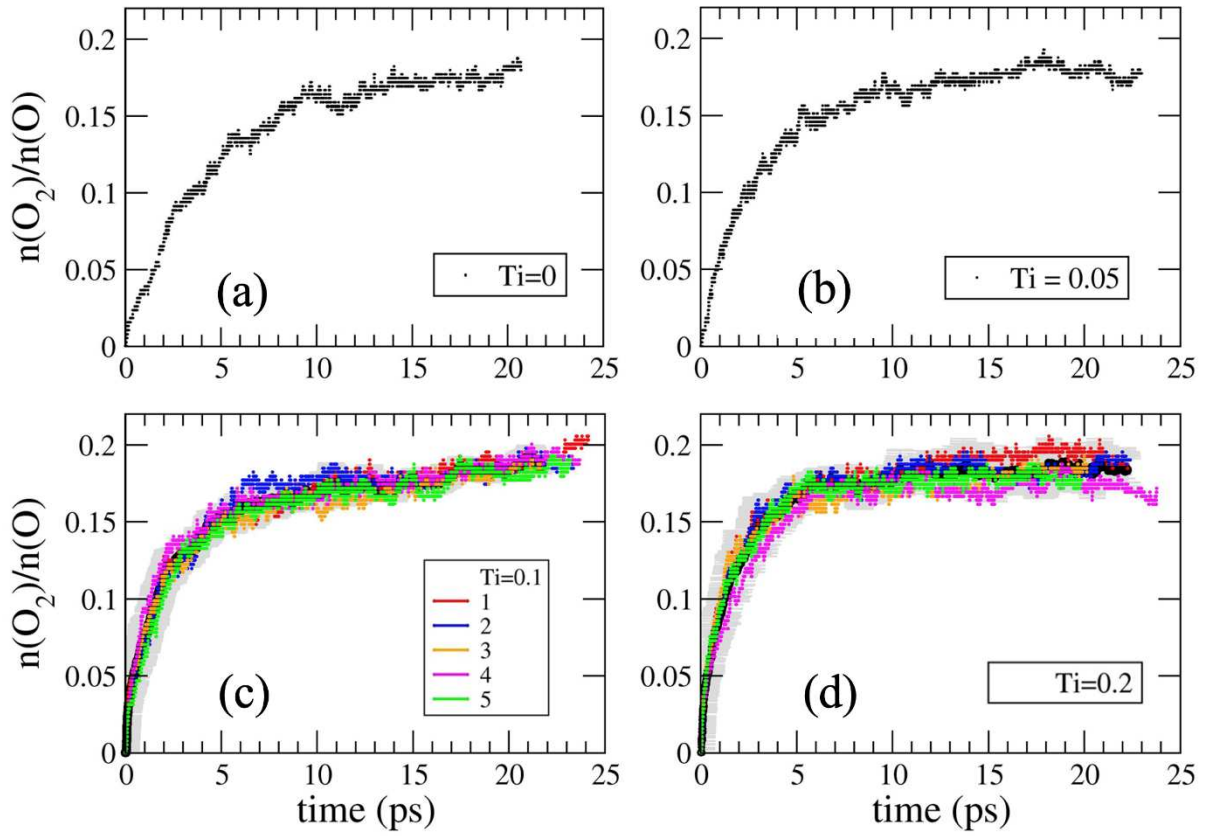


**Figure S19.** O-O dimer fraction with respect to the MD time step for (a) LMO, (b) LMTO-05, (c) LMTO-1 and (d) LMTO-2 at 1000 K. For LMTO-1 and LMTO-2 structures, 5 different MD simulations were performed. The colored lines show the dimer fractions of each structure, and the black line is their average value. The grey color in (c) and (d) show the error bars. Here, time steps are in ps.  $n(\text{O}_2)$  is the total number of dimers and  $n(\text{O})$  is the total number of oxygen atoms in the structures. The dimer fraction is  $n(\text{O}_2)/n(\text{O})$ .

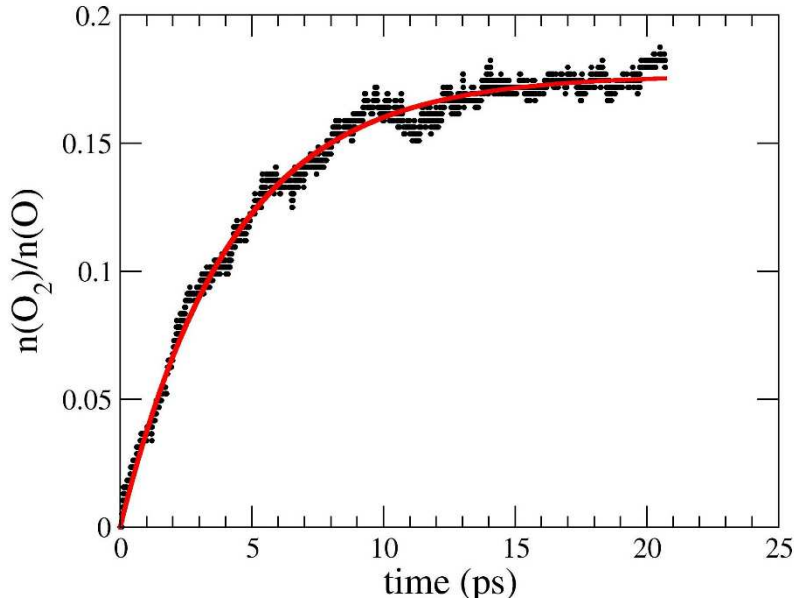


**Figure S20.** O-O dimer fraction with respect to the MD time step for LMO. The red line shows the fitting to equation (2). Here the temperature is 1000 K.

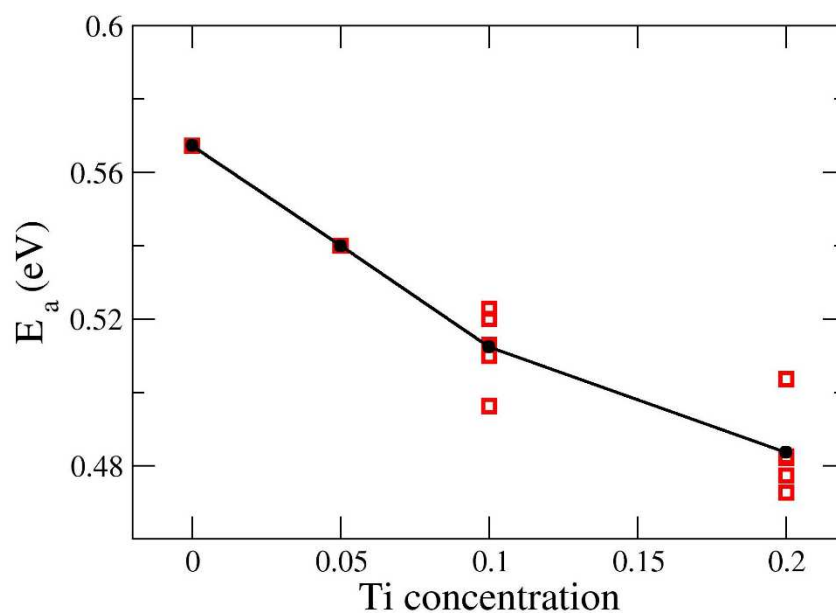


**Figure S21.** Activation energy ( $E_a$ ) with respect to Ti concentration. 0 concentration is LMO, 0.05 concentration is LMTO-05, 0.1 concentration is LMTO-1 and 0.2 concentration is LMTO-2. Red points represent the different configurations for LMTO-1 and LMTO-2. Black line shows the average value for ( $E_a$ ). Here the temperature is 1000 K.

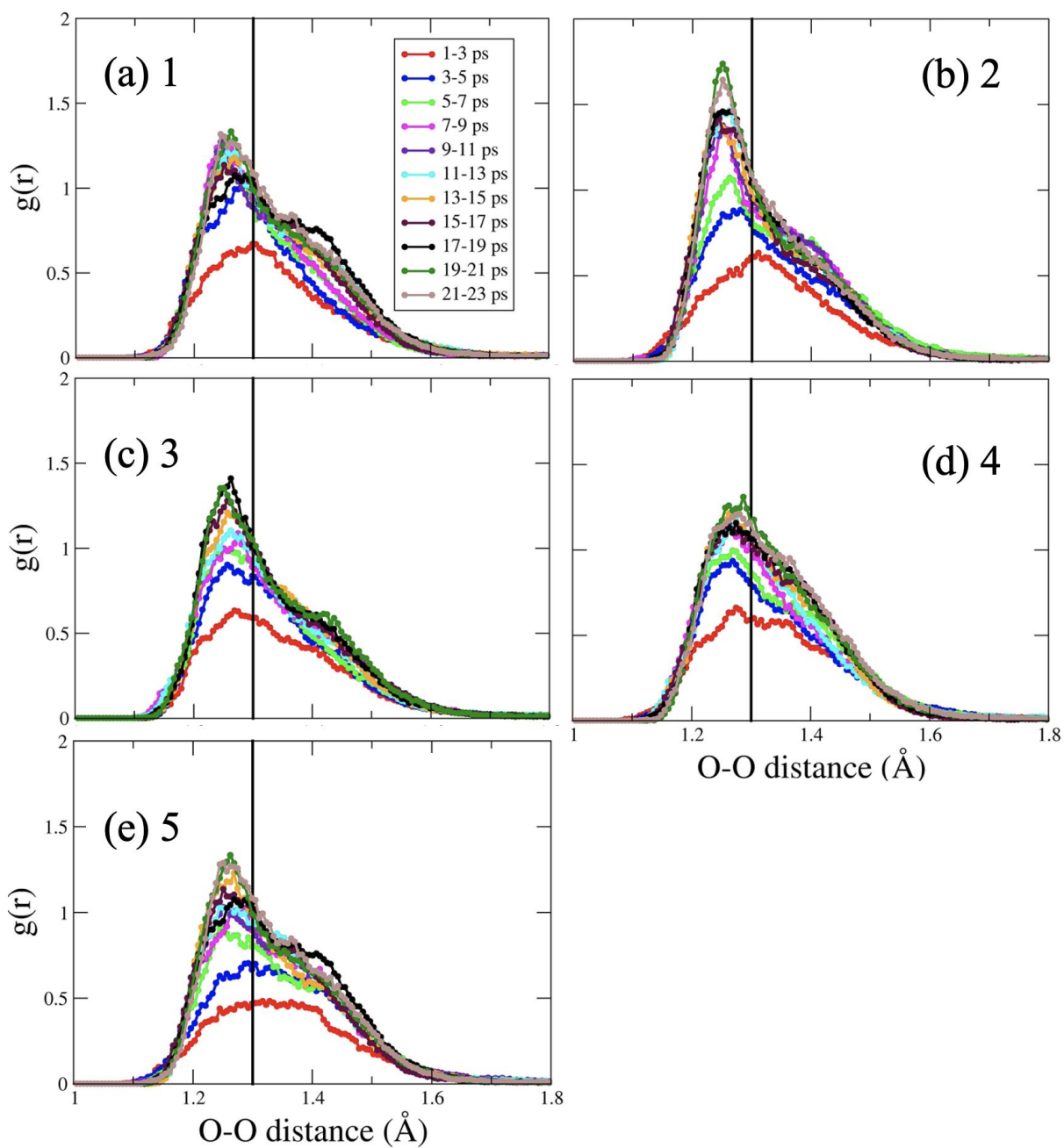


**Figure S22.** Pair distribution function  $g(r)$  with respect to O-O distance for LMTO-1. (a)-(e) the 5 different Ti position configurations. The colored lines show the different time average values. For these calculations, temperature is 1000 K.

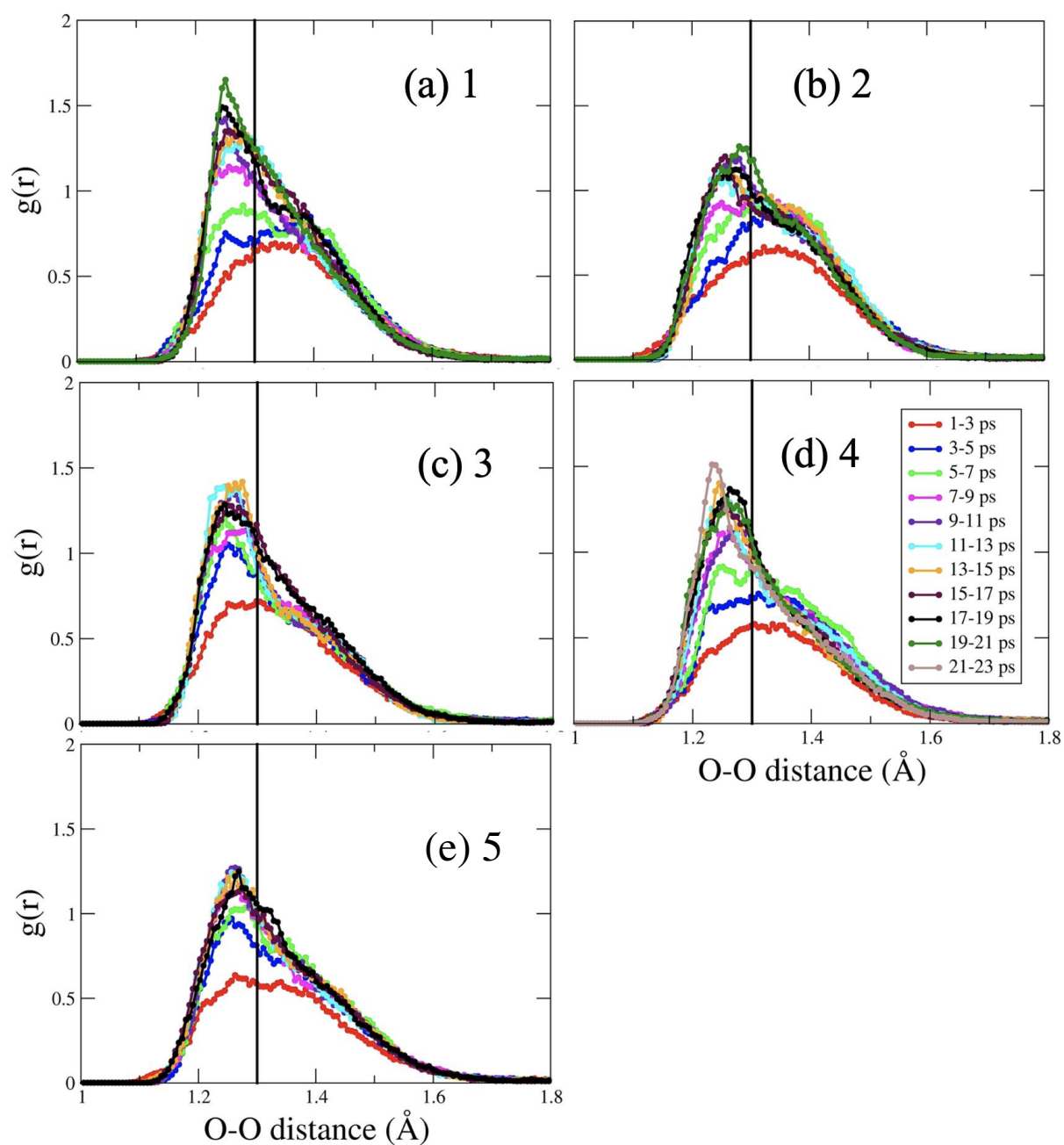


**Figure S23.** Pair distribution function  $g(r)$  with respect to O-O distance for LMTO-2. (a)-(e) the 5 different Ti position configurations. The colored lines show the different time average values. For these calculations, the temperature is 1000 K.

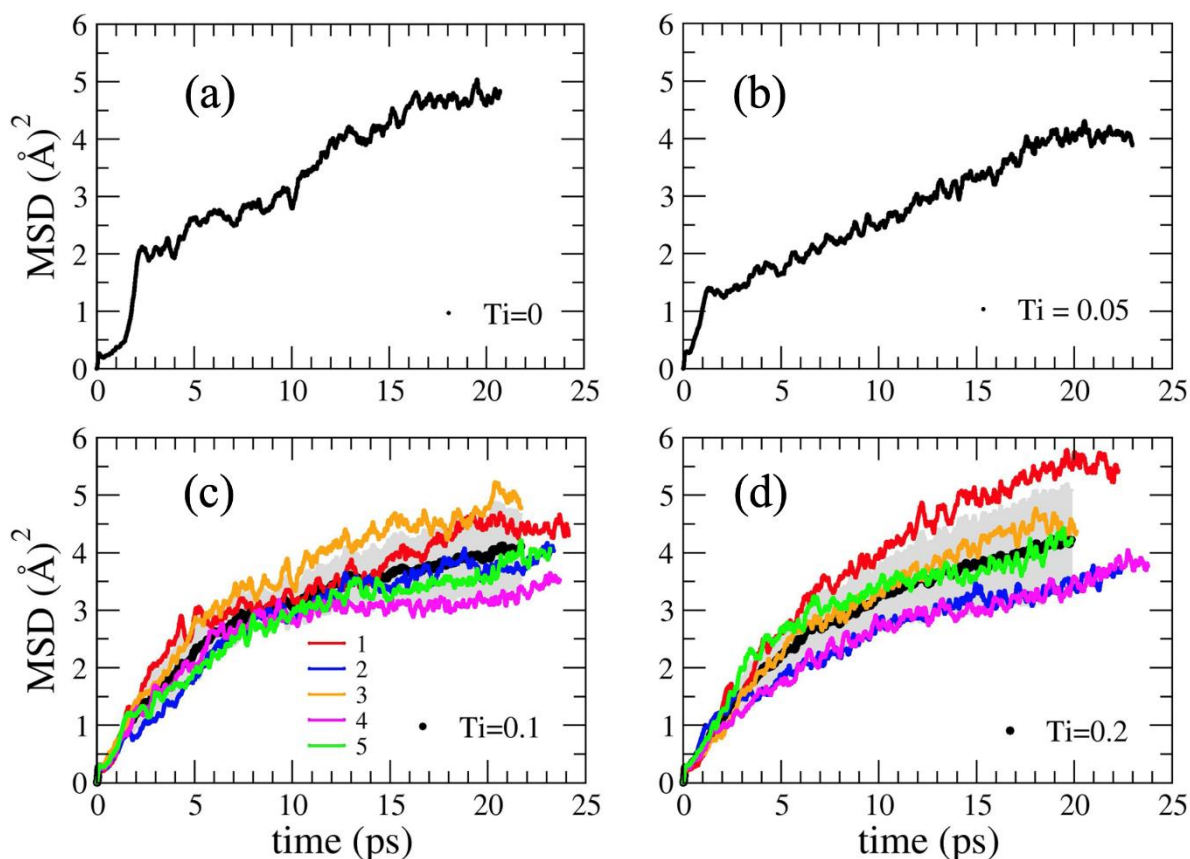


**Figure S24.** Mean square distance (MSD) of Mn atoms with respect to the MD time step for (a) LMO, (b) LMTO-05, (c) LMTO-1 and (d) LMTO-2. For LMTO-1 and LMTO-2 structures, 5 different MD simulations were performed. The colored lines show MSD of each structure, and the black line is their average value. The grey color in (c) and (d) shows the error bars. Here, time steps are in ps and temperature is 1000 K.

- [1] “Fityk --- curve fitting and peak fitting software — Fityk 1.3.1 manual.” <https://fityk.nieto.pl/> (accessed May 05, 2020).
- [2] fengwang, “QSTEM: Quantitative TEM/STEM Simulations — Strukturforschung / Elektronenmikroskopie.” [https://www.physik.hu-berlin.de/en/sem/software/software\\_qstem](https://www.physik.hu-berlin.de/en/sem/software/software_qstem) (accessed May 05, 2020).